

BRIDGING PAST AND FUTURE: DISTRIBUTION-AWARE ALIGNMENT FOR TIME SERIES FORECASTING

Yifan Hu^{1,*}, Jie Yang^{3,*}, Tian Zhou^{2,♣}, Peiyuan Liu¹, Yujin Tang⁴, Rong Jin², Liang Sun^{2,†}

¹Tsinghua University ²DAMO Academy, Alibaba Group

³University of Illinois Chicago ⁴Dartmouth College

{huyf0122, yangjie.workmail, peiyuanliu.edu, tangyujin0275}@gmail.com

{tian.zt, liang.sun}@alibaba-inc.com

ABSTRACT

Although contrastive and other representation-learning methods have long been explored in vision and NLP, their adoption in modern time series forecasters remains limited. We believe they hold strong promise for this domain. To unlock this potential, we explicitly align past and future representations, thereby bridging the distributional gap between input histories and future targets. To this end, we introduce TimeAlign, a lightweight, plug-and-play framework that establishes a new representation paradigm, distinct from contrastive learning, by aligning auxiliary features via a simple reconstruction task and feeding them back into any base forecaster. Extensive experiments across eight benchmarks verify its superior performance. Further studies indicate that the gains arise primarily from correcting frequency mismatches between historical inputs and future outputs. Additionally, we provide two theoretical justifications for how reconstruction improves forecasting generalization and how alignment increases the mutual information between learned representations and predicted targets. Code is in available at <https://github.com/TROUBADOUR000/TimeAlign>.

1 INTRODUCTION

Representation learning techniques have been widely explored for time series forecasting (TSF) (Yue et al., 2022; Eldele et al., 2024; Liu & Chen, 2024; Yang et al., 2025a), inspired by their success in vision (Chen & He, 2021; Yu et al., 2025; Yao et al., 2025) and language tasks (Liu et al., 2023b; Dong et al., 2024). They enable forecasters to gain a deeper understanding of the underlying patterns by automatically deriving efficient representations from time series data. However, for the forecasting task, mapping embeddings extracted from history to future distributions is inherently challenging under distribution shift. *Consequently, models often rely on simplistic direct predictive mappings rather than cultivating richer future-aligned representations, leaving the potential of representation learning largely underexploited in modern forecasters.* We argue that this discrepancy is not merely an implementation issue, but rather stems from a fundamental limitation of the prevailing forecasting paradigm as shown in Fig. 2(a). Below, we thoroughly analyze several failure modes in modern forecasting and propose a novel prediction–reconstruction–alignment solution.

❶ *A shortcut through low-frequency periodicity.* We find that models often exploit this by overemphasizing low-frequency periodic components (Huang et al., 2025; Cai et al., 2024). When representation embeddings are optimized solely under error-driven objectives, such as mean squared error (MSE) or mean absolute error (MAE), the resulting predictions tend to oscillate around the learned mean, following dominant periodic patterns (see Fig. 1(a)). Besides, the similarity within the predicted patches is so high that it indicates the forecast is just a repetition of the low-frequency periodic signals extracted from the past (see Fig. 1(b)). Furthermore, as in Fig. 2(c), our empirical analysis across multiple datasets reveals that high-frequency components in the true values are significant, as they reflect abrupt variations beyond simple periodic repetition and are indispensable for robust forecasting. However, these high-frequency signals are often underestimated in the predictions.

*Equal contribution ♣ Project lead † Corresponding author

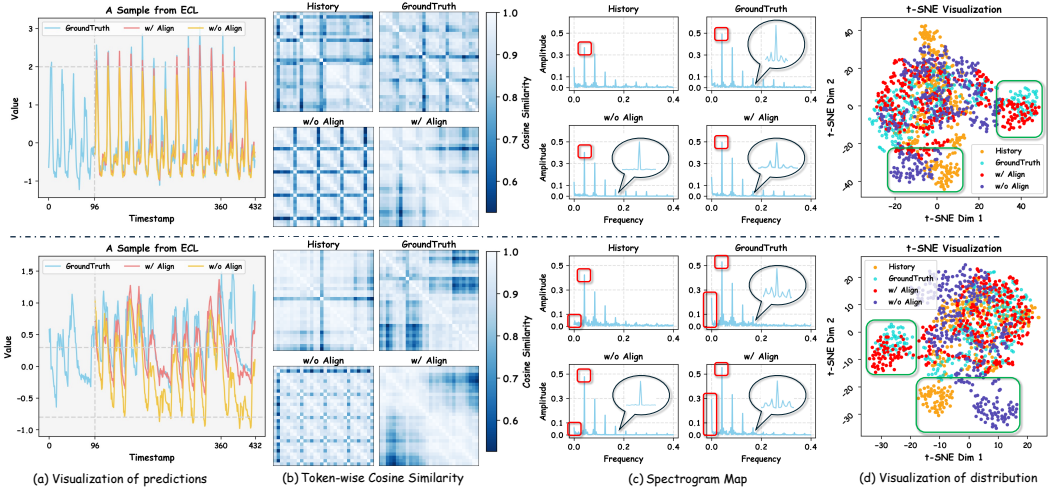


Figure 1: Comparison among history, ground truth, forecast with and without alignment using different visualization perspectives. (a) Time Series Visualization. (b) Token (Patch)-wise Cosine Similarity. (c) Spectrogram Map. (d) t-SNE Embedding Space. More examples are in Sec. F.

② *Distributional mismatch between past and future.* As illustrated in Fig. 1(d), the distribution of learned, high-dimensional representations often differs from the distribution of predicted targets (Kim et al., 2022). In practice, these embeddings tend to favour the statistical characteristics of the past over the future. This discrepancy arises from the inherent shift in distribution between historical sequences and the signals to be forecasted (Fan et al., 2023). Consequently, mapping embeddings extracted from history directly to the target distribution becomes challenging (Dai et al., 2024b; Liu et al., 2023a). To overcome this issue, the representation learning process requires additional constraints to ensure that the learned embeddings faithfully capture historical patterns and are also informative for future prediction.

③ *Structural Flaw of the Unidirectional Paradigm.* Most prevailing prediction paradigm (Fig. 2(a)) is fundamentally unidirectional, mapping historical input solely to the prediction target. This structural constraint inherently limits the model’s ability to retain crucial target information. Consequently, as representations are sequentially encoded through deep layers, the process inadvertently acts like a frequency smoother, discarding subtle frequency structures. And these fine-grained details often encode sudden variations triggered by time-varying external events. After being smoothed out, such information cannot be exploited during forecasting, resulting in a consistently low frequency correlation between predictions and ground truth (see Fig. 2(d)). Therefore, modeling fine-grained dynamics effectively is essential for enhancing robustness against abrupt fluctuations.

Collectively, these three observations underscore fundamental limitations of the current paradigm and thus prompt the following question: *is it possible to design a forecasting framework that can bridge the gap between the past and the future, mitigating distributional shifts while faithfully capturing multi-frequency dynamics?*

To this end, we introduce TimeAlign, which forecasts with an auxiliary reconstruction branch for guidance, as shown in Fig. 2(b), illustrating the prediction–reconstruction–alignment pipeline. The intuition behind reconstruction is twofold. Firstly, unlike forecasting, reconstruction embeddings are naturally aligned with the target distribution since the reconstruction task involves recovering inputs from themselves. Secondly, to faithfully recover signals, reconstruction encourages attention to spectral details, retaining both coarse periodic structures and fine-grained, high-frequency variations. Furthermore, we demonstrate that representations optimized under reconstruction loss exhibit stronger forecasting generalization (see the proof in Sec. B). Consequently, by jointly training the predict and reconstruct branches and aligning their intermediate embeddings, we constrain the predictive representations to be distribution-aware and detail-preserving.

As for alignment, TimeAlign employs two complementary mechanisms. Global alignment reduces the distributional discrepancy between prediction and reconstruction representations, while local alignment enforces fine-grained consistency at the token level. Together, these modules enrich the predictive representation space, enabling the forecaster to capture both periodic low-frequency sig-

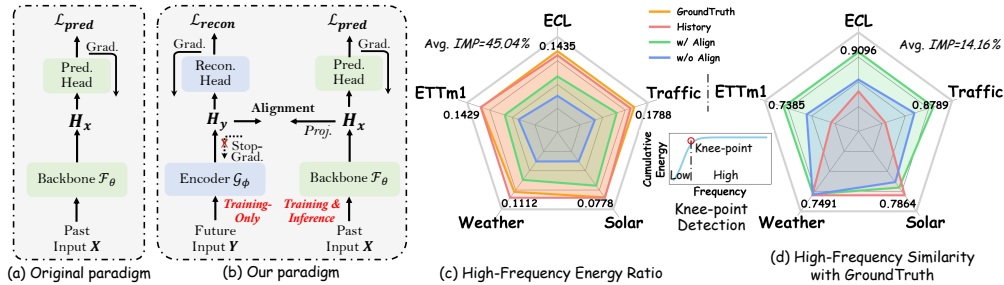


Figure 2: (a) The original paradigm of deep learning forecasters. Distributions are extracted from history and mapped to the prediction space. (b) The paradigm of TimeAlign. Joint optimization of the predict and reconstruct branches provides distributional alignment. (c) High-frequency energy ratio. For different datasets, the threshold between high- and low-frequency bands is determined adaptively via knee-point detection of the cumulative energy distribution. (d) High-frequency similarity. Pearson correlations are computed on the high-frequency components between the ground truth and the history, the forecast with and without alignment. *IMP*. means improvement.

nals and high-frequency dynamics. Importantly, alignment reflects a deeper principle. Predictive representations inherently contain mutual information with future targets, yet conventional objectives underutilize it. Our analyses confirm that TimeAlign acts as an implicit mutual information enhancer, aligning predictive representations more closely with targets (see the proof in Sec. C).

Extensive experiments demonstrate TimeAlign effectively bridges past and future and delivers more reliable forecasts across diverse datasets. In a nutshell, our contributions are summarized as follows:

- ① **Paradigm Shift.** We revisit the representation learning in the current dominant forecasting paradigm and reveal its key limitations. It overemphasizes low-frequency periodicity, suffers from distribution mismatch, and discards informative fine-grained components. To fill these gaps, we introduce a new paradigm incorporating alignment between prediction and reconstruction.
- ② **Technical Contribution.** We present TimeAlign, a dual-branch framework that consists of a predict branch and a reconstruct branch, distribution-aware aligning their latent representations through global and local objectives to bridge the past and future effectively.
- ③ **In Theory and In Practice.** We provide two theoretical guarantees: (i) reconstruction improves the forecasting generalization, and (ii) alignment enhances the mutual information between predictive representations and future targets. Extensive experiments across diverse benchmarks further validate these insights, establishing state-of-the-art performance in both accuracy and robustness.

2 RELATED WORKS

2.1 DEEP LEARNING IN TIME SERIES FORECASTING

Recently, deep learning has become the dominant paradigm for TSF, with a variety of neural architectures including CNN (Donghao & Xue, 2024; Wu et al., 2023; Wang et al., 2022), Linear (Huang et al., 2025; Hu et al., 2025c; Si et al., 2025), Transformer (Liu et al., 2024b; 2025; Dai et al., 2024a), GNN (Hu et al., 2025d; Wu et al., 2020), etc. Despite architectural diversity, these methods generally follow an encoder–decoder paradigm: they embed historical sequences into latent representations and map them to predictive targets (see Fig. 2(a)). However, as shown in Fig. 1, this paradigm tends to overemphasize low-frequency patterns while neglecting fine-grained structures, and it suffers from distribution mismatch between history and future. To address these limitations, we propose TimeAlign, which jointly optimizes predict and reconstruct branches and aligns their embeddings, thereby bridging the gap between the past and the future more effectively.

2.2 REPRESENTATION LEARNING

Representation learning is crucial for enabling models to capture meaningful and transferable features. Across domains, it has been used to introduce inductive biases that extend beyond task-specific objectives. For instance, in diffusion models, learned representations serve as structured noise priors that improve sample quality and stability (Yang et al., 2025c; Yu et al., 2025; Jiang et al., 2025), while in vision and language, aligning task-specific embeddings with pre-trained ones

enriches feature spaces and boosts downstream performance (Yao et al., 2025; Leng et al., 2025). However, in TSF, error-driven training often yields biased embeddings that smooth away subtle but critical dynamics Yue et al. (2022); Eldele et al. (2024), limiting their predictive value. We argue that auxiliary mechanisms are needed to enforce consistency between predictive and reconstructive signals, thereby preserving fine-grained temporal cues and alleviating distribution mismatch.

3 METHOD

3.1 PROBLEM DEFINITION

In TSF task, let $\mathbf{X} = \{x_1, x_2, \dots, x_C\} \in \mathbb{R}^{C \times L}$ be the history input series, where C denotes the number of channels and L denotes the look-back horizon. $\mathbf{x}_i \in \mathbb{R}^L$ represents one of the channels. The objective is to construct a model $\mathcal{F}_\theta(\cdot)$ that predicts the future sequences $\hat{\mathbf{Y}}_{\text{pred}} \in \mathbb{R}^{C \times T}$, where T denotes the forecasting horizon. The forecasting process is given by $\hat{\mathbf{Y}}_{\text{pred}} = \mathcal{F}_\theta(\mathbf{X})$. A lower error between $\hat{\mathbf{Y}}_{\text{pred}}$ and ground truth \mathbf{Y} indicates stronger forecasting capability of the model $\mathcal{F}_\theta(\cdot)$. However, \mathbf{X} and \mathbf{Y} often exhibit distribution shift. Instead of predicting patterns in \mathbf{Y} using learnable statistics derived from \mathbf{X} , our focus is to leverage direct constraint from \mathbf{Y} to guide model optimization, thereby achieving robust and efficient distribution alignment between $\hat{\mathbf{Y}}_{\text{pred}}$ and \mathbf{Y} . To this end, we introduce an auxiliary reconstruction task. Specifically, the reconstruction model is defined as $\mathcal{G}_\phi(\cdot)$ that directly maps \mathbf{Y} to its reconstruction $\hat{\mathbf{Y}}_{\text{recon}} = \mathcal{G}_\phi(\mathbf{Y})$. Here, $\mathcal{G}_\phi(\cdot)$ learns a compact representation of the target distribution without relying on past inputs, and the reconstruct representation \mathbf{H}_y serves as a guidance for aligning the latent space \mathbf{H}_x of $\mathcal{F}_\theta(\cdot)$.

3.2 STRUCTURE OVERVIEW

As illustrated in Fig. 3, our proposed TimeAlign consists of four components: (i) **Predict Branch** employs a backbone encoder to map \mathbf{X} to $\hat{\mathbf{Y}}_{\text{pred}}$, active in both training and inference. The backbone is *plug-and-play* and replaceable by any forecasting architecture. In our default setup, it shares the same lightweight encoder as the Reconstruct Branch to highlight the effect of alignment. (ii) **Reconstruct Branch** leverages a lightweight encoder to reconstruct $\hat{\mathbf{Y}}_{\text{recon}}$ from \mathbf{Y} , thereby capturing a compact representation aligned with the target distribution. This branch is used only during training. (iii) **Distribution-Aware Alignment** explicitly aligns \mathbf{H}_x and \mathbf{H}_y via global and local mechanisms, providing distributional constraint for optimization. (iv) **A Simple Encoder** serves as the minimal yet effective design for the Reconstruct Branch and default Predict Branch.

3.3 PREDICT BRANCH

The predict branch follows the standard deep learning paradigm for TSF, extracting temporal representations from historical input and mapping them into the future horizon. In TimeAlign, we deliberately adopt a minimal encoder design to demonstrate that the improvements stem from alignment rather than architectural complexity. Importantly, the encoder here can be replaced by more sophisticated backbones, enabling TimeAlign to serve as a plug-and-play module.

Given the history input $\mathbf{X} \in \mathbb{R}^{C \times L}$, we first divide it into patches and project them onto embeddings $\mathbf{X}_p = \text{Linear}(\text{Patching}(\mathbf{X})) \in \mathbb{R}^{(C \cdot N) \times D}$, where N is the number of patches and the Reconstruct Branch share the same N with the Predict Branch. \mathbf{X}_p is then processed by an M -layer encoder, where each layer consists of a linear–activation–linear block with residual connection:

$$\mathbf{H}_x^l = \mathbf{H}_x^{l-1} + \text{Linear}(\sigma(\text{Linear}(\mathbf{H}_x^{l-1}))), \quad l = 1, \dots, M \quad (1)$$

with $\mathbf{H}_x^0 = \mathbf{X}_p$ and σ is an activation function. Finally, a prediction head projects the latent representation into the forecasting results $\hat{\mathbf{Y}}_{\text{pred}} = \text{Linear}(\mathbf{H}_x^M)$.

3.4 RECONSTRUCT BRANCH

The reconstruct branch provides explicit constraint from the target distribution by reconstructing the ground truth from itself. This design captures the intrinsic structure of \mathbf{Y} , thereby offering a reliable

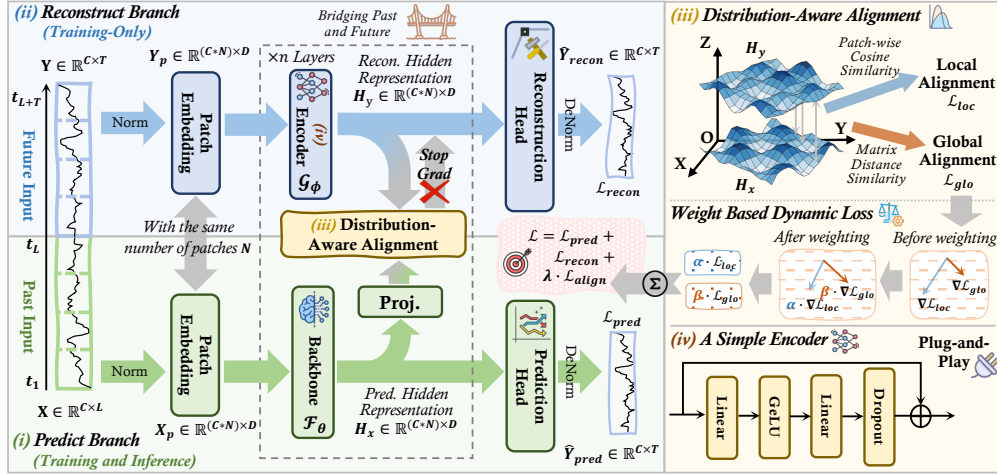


Figure 3: Overall architecture of TimeAlign. (i) **Predict Branch** maps history to forecasts (both training and inference), with a *replaceable* backbone. (ii) **Reconstruct Branch** reconstructs targets to capture the distribution (training-only). (iii) **Distribution-Aware Alignment** aligns predict and reconstruct representations via global and local mechanisms. (iv) **A Simple Encoder** is the default lightweight design in Reconstruct Branch and default Predict Branch.

distributional \mathbf{H}_y reference for alignment. Unlike the predict branch, the reconstruct branch is only active during training and discarded at inference.

Similarly, given the future sequence $\mathbf{Y} \in \mathbb{R}^{C \times T}$, we embed it in the same way of patch embedding $\mathbf{Y}_p = \text{Linear}(\text{Patching}(\mathbf{Y})) \in \mathbb{R}^{(C \cdot N) \times D}$. It is then encoded by the same M -layer encoder:

$$\mathbf{H}_y^l = \mathbf{H}_y^{l-1} + \text{Linear}(\sigma(\text{Linear}(\mathbf{H}_y^{l-1}))), \quad l = 1, \dots, M \quad (2)$$

with $\mathbf{H}_y^0 = \mathbf{Y}_p$. Finally, a reconstruction head then maps the latent representation back into the target space $\hat{\mathbf{Y}}_{\text{recon}} = \text{Linear}(\mathbf{H}_y^M)$.

The hidden representations H_x and H_y are structured by deep transformations and normalization layers. In the spirit of the Central Limit Theorem (CLT), these compounding effects typically enforce the distribution of H_x and H_y to be approximately Gaussian. This structured property is key to the theoretical generalization advantages discussed in Sec. B.

3.5 DISTRIBUTION-AWARE ALIGNMENT

Although the predict and reconstruct branches encode their respective inputs independently, the latent spaces still diverge due to distributional shift between the history \mathbf{X} and the target \mathbf{Y} . To explicitly bridge this gap, we introduce a distribution-aware alignment module that aligns the representations of the two branches at each layer. We consider the i -th layer as an example below.

Alignment with an Additional Mapping. Instead of aligning the raw hidden states directly, we introduce an additional linear mapping applied to the predict branch before alignment:

$$\tilde{\mathbf{H}}_x^i = \text{Linear}(\mathbf{H}_x^i) \in \mathbb{R}^{(C \cdot N) \times D}. \quad (3)$$

This mapping layer, implemented as a lightweight Linear layer, serves to temporally reposition and normalize the highly abstracted features of the predict branch, making them more compatible with the representations from the reconstruct branch. Importantly, gradients from the alignment loss are only propagated to the predict branch via this Linear layer, leaving the reconstruct branch unaffected (Chen & He, 2021). This asymmetric gradient flow ensures that the reconstruct branch provides a stable supervisory signal without being distorted by the alignment procedure.

Local vs. Global Complementarity. To ensure fine-grained fidelity and distributional consistency, we introduce two complementary objectives, including local alignment to capture patch-wise similarity and global alignment to capture relational structure (Yao et al., 2025; Yang et al., 2025b).

Local alignment ensures that individual patch-level features capture similar semantics, while global alignment enforces consistency in the overall relational structure of representations (Yang et al., 2026). Specifically, local alignment preserves fine-grained similarity between corresponding patches, which is crucial for capturing sharp transitions and high-frequency details. Notably, such similarity measures spectral energy projection, thereby leveraging multi-frequency information. $h_{x,j}^i$ is the j -th item in \mathbf{H}_x^i and $n = C \cdot NL$:

$$\mathcal{L}_{\text{local}}^i = \frac{1}{n^2} \sum_{j=1}^n \text{GELU} \left(1 - \left| \tilde{h}_{x,j}^i \cdot h_{y,j}^i \right| - \delta_{loc} \right). \quad (4)$$

Meanwhile, global alignment aims to make the relative distance matrices within the features as similar as possible, ensuring that large-scale temporal dependencies and low-frequency dynamics are also aligned. \top means the transpose. We subtract margins δ_{loc} and δ_{glo} to relax the constraint:

$$\mathcal{L}_{\text{global}}^i = \frac{1}{n^2} \sum_{j=1}^n \text{GELU} \left(\left\| \tilde{h}_{x,j}^i (\tilde{h}_{x,j}^i)^\top - h_{y,j}^i (h_{y,j}^i)^\top \right\|_1 - \delta_{glo} \right). \quad (5)$$

These margins are used to relax the constraint, which is a common technique in metric learning. They create a ‘‘buffer’’ where, if two representations are already close enough, the loss becomes zero. This prevents the model from overfitting on easy samples and focuses its optimization effort on harder-to-align pairs, leading to more stable training.

Weight-Based Dynamic Loss. Finally, the overall alignment objective is a weighted fusion

$$\mathcal{L}_{\text{align}} = \frac{1}{M} \sum_{i=1}^M (\alpha \mathcal{L}_{\text{local}}^i + \beta \mathcal{L}_{\text{global}}^i). \quad (6)$$

We adopt an adaptive scheme to prevent domination of either objective and stabilizes optimization across different datasets and regimes. The dynamic weights α and β are computed as

$$\alpha = \frac{\mathcal{L}_{\text{local}} + \mathcal{L}_{\text{global}}}{\mathcal{L}_{\text{local}}}, \quad \beta = \frac{\mathcal{L}_{\text{local}} + \mathcal{L}_{\text{global}}}{\mathcal{L}_{\text{global}}}. \quad (7)$$

Combining local and global alignment under an asymmetric mapping design encourages the predict branch to capture detailed, patch-level similarities while respecting global relational structures. This dual alignment, guided by the stable target distribution from the reconstruct branch, enhances the robustness and fidelity of the forecasting process.

3.6 OPTIMIZATION OBJECTIVE

The full optimization combines the prediction loss, reconstruction loss, and alignment loss:

$$\mathcal{L} = \mathcal{L}_{\text{pred}} + \mathcal{L}_{\text{recon}} + \lambda \mathcal{L}_{\text{align}} \quad (8)$$

where $\mathcal{L}_{\text{pred}}$ and $\mathcal{L}_{\text{recon}}$ are error-based MAE objectives and λ is a scaling weight. This joint training paradigm enables the predict branch to benefit directly from distributional constraint provided by the reconstruct branch.

4 THEORETICAL ANALYSIS

4.1 IMPROVE GENERALIZATION WITH RECONSTRUCTION ERROR MINIMIZATION

The following theorem characterizes the advantage of reconstruction-guided estimation. Let \mathcal{M}^* be the optimal forecasting solution, \mathcal{M}_1 the empirical estimator obtained from the training examples, and \mathcal{M}_2 the estimator derived from the one-dimensional representation via reconstruction error minimization. Given the concentration bounds, the reconstruction-based estimator \mathcal{M}_2 achieves a strictly tighter approximation to \mathcal{M}^* than \mathcal{M}_1 . The proof can be found in Sec. B.

$$\frac{|\mathcal{M}_2 - \mathcal{M}^*|_F}{|\mathcal{M}^*|_F} \ll \frac{|\mathcal{M}_1 - \mathcal{M}^*|_F}{|\mathcal{M}^*|_F} \quad (9)$$

where $|\cdot|_F$ denotes the Frobenius norm.

4.2 TIMEALIGN IS AN IMPLICIT MUTUAL INFORMATION ENHANCER

To understand the mechanism of $\mathcal{L}_{\text{align}}$ from a structural perspective, we reformulate the role of our dual loss objectives through the lens of Mutual Information Maximization (MIM). The conventional prediction loss, $\mathcal{L}_{\text{pred}}$, provides a variational lower bound on the mutual information $I(\mathbf{Y}; \mathbf{H}_x)$, implicitly guiding the representation learning. Our core alignment of TimeAlign acts as a complementary mechanism, ensuring that the predictive representation $\mathbf{H}_x(h_x)$ is explicitly enriched by maximizing its mutual information with the ground truth $\mathbf{Y}(y)$. This effectively enhances the total information flow used for forecasting. The mutual information is formulated as:

$$I(\mathbf{Y}; \mathbf{H}_x) = \mathbb{E}_{p(y, h_x)} \left[\log \frac{p(y, h_x)}{p(h_x) \cdot p(y)} \right]. \quad (10)$$

MIM in Prediction Loss. Following the derivations introduced in previous IB-relevant works (Choi & Lee, 2023; Alemi et al., 2016), we can obtain a lower bound for the informative term, which aims to maximize the mutual information between \mathbf{H}_x and \mathbf{Y} (see full derivation in Sec. C.1):

$$\begin{aligned} I(\mathbf{Y}; \mathbf{H}_x) &= \mathbb{E}_{p(y, h_x)} \left[\log \frac{\mathcal{F}_\theta(y|h_x)}{p(y)} \right] + \int_{h_x} p(h_x) \cdot D_{\text{KL}}[p(y|h_x) || \mathcal{F}_\theta(y|h_x)] dh_x \\ &\geq \mathbb{E}_{p(y, h_x)} [\log \mathcal{F}_\theta(y|h_x)] \stackrel{\text{def}}{=} -\mathcal{L}_{\text{pred}}, \end{aligned} \quad (11)$$

where the inequality holds due to the non-negativity of the KL divergence and entropy.

MIM in Alignment Loss. To further enhance the mutual information, we introduce a complementary formulation that explicitly targets the mutual information between \mathbf{H}_x and \mathbf{Y} . Inspired by the InfoNCE objective from contrastive learning (Oord et al., 2018), we derive an alternative lower bound of $I(\mathbf{Y}; \mathbf{H}_x)$ (see the full derivation in Sec. C.2). Furthermore, instead of predicting y directly, we model a density ratio $f(y, h_x) = \exp(\text{proj}(h_x)^\top \cdot \mathcal{G}_\phi(y))$ that preserves mutual information $I(Y; Z)$, as it is proportional to $\frac{p(y|z)}{p(y)}$. This yields the following Alignment loss.

$$\begin{aligned} I(\mathbf{Y}; \mathbf{H}_x) &= -\mathbb{E}_{p(y, h_x)} \left[\log \left(\frac{p(y)}{p(y|h_x)} \cdot N \right) - \log N \right] \approx -\mathbb{E}_{p(y, h_x)} \left[\log \left(\frac{p(y)}{p(y|h_x)} \cdot N \right) \right] \\ &= -\mathbb{E}_{p(y, h_x)} [\exp(\text{proj}(h_x)^\top \cdot \mathcal{G}_\phi(y))] \stackrel{\text{def}}{=} -\mathcal{L}_{\text{align}}. \end{aligned} \quad (12)$$

In summary, jointly optimizing $\mathcal{L}_{\text{pred}}$ and $\mathcal{L}_{\text{align}}$ effectively maximizes the mutual information $I(\mathbf{Y}; \mathbf{H}_x)$, thereby enabling more accurate and robust representation learning. To further refine $\mathcal{L}_{\text{align}}$, we adopt the complementary local and global strategies discussed in Sec. 3.5, which together ensure both fine-grained fidelity and distributional consistency.

5 EXPERIMENT

In this section, we conduct extensive experiments to validate the superiority of our TimeAlign in **effective forecasting performance**, **plug-and-play capability**, and **competitive efficiency**. More experimental details can be found in Sec. D and Sec. E.

5.1 EXPERIMENT SETUP

Datasets. We conduct experiments on eight widely used real-world datasets, including the Electricity Transformer Temperature (ETT) dataset with its four subsets (ETTh1, ETTh2, ETTm1, ETTm2), as well as Weather, Electricity, Traffic, and Solar (Miao et al., 2025; 2024). The statistics of the datasets are shown in Sec. D.2.

Baselines. We compare TimeAlign with several SOTA baselines representing the latest advances in TSF, including TimeMixer (Wang et al., 2024), iTransformer (Liu et al., 2024b), PatchTST (Nie et al., 2023), Crossformer (Zhang & Yan, 2023), TVNet (Li et al., 2025), ModernTCN (Donghao & Xue, 2024), TimesNet (Wu et al., 2023), and lightweight methods like DLinear (Zeng et al., 2023), CMoS (Si et al., 2025), TimeBase (Huang et al., 2025) and Leddam (Yu et al., 2024).

Models	TimeAlign (Ours)		CMoS (2025)		TimeBase (2025)		TVNet (2025)		iTransformer (2024b)		TimeMixer (2024)		Leddam (2024)		ModernTCN (2024)		PatchTST (2023)		Crossformer (2023)		TimesNet (2023)		DLinear (2023)	
	MSE	MAE	MSE	MAE	MSE	MAE	MSE	MAE	MSE	MAE	MSE	MAE	MSE	MAE	MSE	MAE	MSE	MAE	MSE	MAE	MSE	MAE	MSE	MAE
ETTm1	0.340	0.367	0.354	<u>0.378</u>	0.357	0.380	<u>0.348</u>	0.379	0.362	0.391	0.355	0.380	0.354	0.381	0.351	0.381	0.353	0.382	0.420	0.435	0.400	0.406	0.356	<u>0.378</u>
ETTm2	0.243	0.302	0.259	0.316	<u>0.250</u>	0.314	0.251	<u>0.311</u>	0.269	0.329	0.257	0.318	0.265	0.320	0.253	0.314	0.256	0.317	0.518	0.501	0.292	0.330	0.259	0.324
ETTh1	0.406	0.420	<u>0.403</u>	<u>0.416</u>	0.396	0.414	0.407	0.421	0.439	0.448	0.427	0.441	0.415	0.430	0.404	0.420	0.418	0.436	0.440	0.463	0.458	0.450	0.424	0.439
ETTh2	0.336	0.382	0.331	0.383	0.345	0.397	<u>0.324</u>	0.377	0.374	0.406	0.349	0.397	0.345	0.391	0.322	<u>0.379</u>	0.351	0.404	0.809	0.658	0.390	0.427	0.431	0.447
Weather	0.214	0.244	0.220	<u>0.261</u>	<u>0.219</u>	0.263	0.221	<u>0.261</u>	0.233	0.271	0.226	0.264	0.226	0.264	0.224	0.264	0.226	0.264	0.228	0.287	0.259	0.287	0.242	0.293
Electricity	0.154	0.244	0.158	<u>0.250</u>	0.167	0.258	0.165	0.254	0.164	0.261	0.185	0.284	0.162	0.256	<u>0.156</u>	0.253	0.159	0.253	0.181	0.279	0.192	0.295	0.166	0.264
Traffic	0.378	0.240	<u>0.396</u>	0.270	0.417	0.278	<u>0.396</u>	<u>0.268</u>	0.397	0.282	0.409	0.279	0.452	0.283	<u>0.396</u>	0.270	0.397	0.275	0.523	0.284	0.620	0.336	0.418	0.287
Solar	0.192	0.214	0.210	0.257	0.236	0.270	0.228	0.277	0.202	0.248	<u>0.193</u>	0.264	0.223	0.264	0.228	0.281	0.194	0.245	0.205	<u>0.232</u>	0.244	0.334	0.224	0.226

Table 1: Long-term forecasting results. The input length L is searched from $\{336, 512, 720\}$ and the results are averaged across four forecasting horizons $T \in \{96, 192, 336, 720\}$. The best and second-best results are highlighted in **bold** and underlined, respectively. See Tab. 6 for full results.

Case	Local Align		Global Align		ETTm1		ETTm2		Weather		Electricity		Traffic	
	w/	w/	w/	w/	MSE	MAE								
①	×	×	×	×	0.349	0.370	0.252	0.308	0.225	0.254	0.159	0.248	0.390	0.249
②	✓	×	×	×	0.344	0.372	0.245	0.305	0.220	0.249	<u>0.157</u>	0.247	<u>0.383</u>	<u>0.244</u>
③	×	✓	✓	✓	<u>0.342</u>	<u>0.369</u>	<u>0.244</u>	<u>0.303</u>	<u>0.218</u>	<u>0.247</u>	<u>0.157</u>	<u>0.246</u>	<u>0.383</u>	0.245
④	✓	✓	✓	✓	0.340	0.367	0.243	0.302	0.214	0.244	0.154	0.244	0.378	0.240

Table 2: Full results of ablation on the effect of removing alignment in local and global perspective. ✓ indicates the use of alignment, while × means alignment is retained.

Implementation Details. All experiments are performed on one NVIDIA V100 32GB GPU. We select two common metrics in TSF: MAE and MSE. Moreover, a grid search is conducted on the look-back length of $\{96, 192, 336, 512, 720\}$. For each setting, the results are averaged over three runs with random seeds. For additional details on hyperparameters, please refer to Sec. D.3.

5.2 FORECASTING PERFORMANCE

As shown in Tab. 1, TimeAlign delivers **effective forecasting performance** across most datasets. The only exceptions are ETTh1 and ETTh2, yet its performance remains highly competitive. Most notably, on the ETTm1 and ETTm2 datasets known for severe distribution shifts (Qiu et al., 2024), TimeAlign substantially outperforms current SOTA methods. Owing to the Distribution-Aware Alignment Module, TimeAlign aligns predict representations with evolving distributions, thereby enabling more detailed modeling of the target and further boosting accuracy. Overall, compared to the second best method TVNet, TimeAlign reduces MSE/MAE by 3.27%/5.20%, with a Wilcoxon test p-value of $1.37e^{-8}$ confirming significance at 99% confidence. The full error bars are in Tab. 7.

5.3 ABLATION STUDIES

We validate the effectiveness of each architectural design in TimeAlign through the following ablation studies: ① **w/o Align** signifies the Predict Branch alone without alignment. ② **w/ Local only** denotes the Local Alignment is retained. ③ **w/ Global only** denotes only the Global Alignment is retained. ④ **w/ Align** encompasses both Local and Global Alignment mechanisms.

The results in Tab. 2 reveal that the combination of Local and Global Alignment is essential for accurately reconciling the predict representations with the target distribution, yielding the best performance. Interestingly, Global Alignment alone outperforms Local Alignment alone; the former provides a coarse-grained distribution-level pull that is more effective at high-level representation calibration, while the latter focuses on fine-grained, point-wise corrections. As expected, removing both alignment strategies results in the worst accuracy. Furthermore, we observe that w/o Align is already a SOTA-level Baseline, showing that TimeAlign achieves consistent performance improvements on top of the already-SOTA-level baseline. This proves that our TimeAlign module is not a trick that only works on a weak baseline. It is a powerful module that can take a strong, efficient, SOTA-level architecture and make it even better.

Additionally, the effectiveness of Reconstruct can be found in Sec. E.5.

Models	iTransformer			+TimeAlign				DLinear			+TimeAlign			
	MSE	MAE	SIM	MSE	MAE	SIM	ΔIMP	MSE	MAE	SIM	MSE	MAE	SIM	ΔIMP
ETTm1	0.362	0.391	0.862	0.355	0.384	0.865	+1.80%	0.356	0.378	0.869	0.352	0.373	0.872	+1.05%
ETTm2	0.269	0.329	0.970	0.260	0.317	0.974	+3.44%	0.259	0.324	0.973	0.252	0.311	0.976	+2.61%
ETTh1	0.439	0.448	0.825	0.428	0.448	0.828	+2.45%	0.424	0.439	0.841	0.414	0.433	0.840	+2.41%
ETTh2	0.374	0.406	0.958	0.363	0.402	0.962	+2.87%	0.431	0.447	0.960	0.418	0.431	0.960	+3.07%
Weather	0.233	0.271	0.777	0.240	0.274	0.777	-3.00%	0.242	0.293	0.778	0.238	0.280	0.775	+1.55%
Electricity	0.164	0.261	0.914	0.163	0.255	0.916	+0.76%	0.166	0.264	0.912	0.164	0.260	0.916	+1.20%
Traffic	0.397	0.282	0.845	0.390	0.260	0.848	+1.95%	0.418	0.287	0.832	0.418	0.285	0.833	+0.12%
Solar	0.202	0.248	0.852	0.204	0.243	0.853	-0.87%	0.224	0.226	0.848	0.214	0.219	0.852	+4.15%

Table 3: Full results of long-term forecasting with TimeAlign as a plugin. All results are averaged across four different prediction lengths: $O \in \{96, 192, 336, 720\}$. ΔIMP denotes TimeAlign’s performance gain, either *positive* or *negative*.

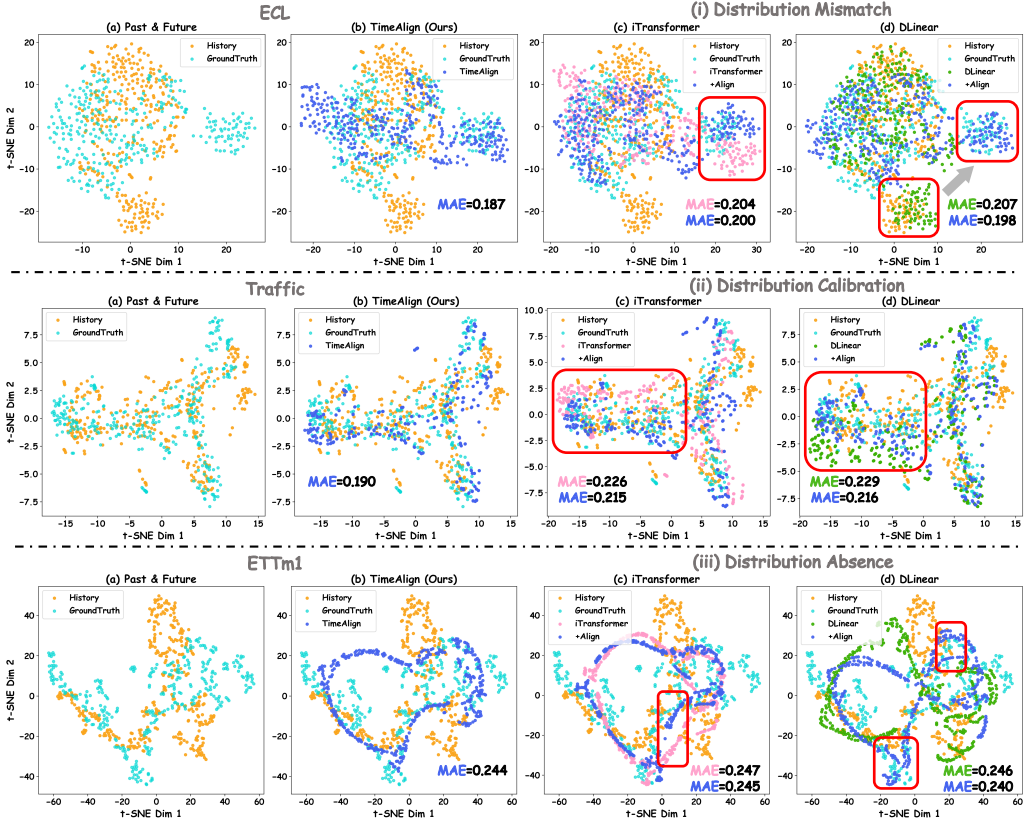


Figure 4: The t-SNE visualization illustrates the distribution of the history, the ground truth and the forecasts produced by TimeAlign, iTransformer (Liu et al., 2024b), DLinear (Zeng et al., 2023), iTransformer+TimeAlign and DLinear+TimeAlign on the ECL, Traffic, and ETTm1 datasets. The TimeAlign forecasts almost perfectly overlap with the ground truth manifold, whereas the predictions from vanilla iTransformer and DLinear exhibit obvious distributional divergence. Plugging in TimeAlign visibly collapses this gap, steering backbones toward the target distribution.

5.4 PLUG-AND-PLAY EXPERIMENT

TimeAlign can be seamlessly integrated into diverse forecasting backbones. For encoder-based models, the encoder first maps the history X into a latent embedding X' via patch embedding (Nie et al., 2023), value-wise convolution (Liu et al., 2024b; Wu et al., 2021), or linear projection (Huang et al., 2025). A parallel reconstruct branch with the same architecture projects the target Y into the same space Y' , enabling alignment between prediction and reconstruction representations. This guides the backbone beyond point-wise error minimization toward representations more informative of the target. To verify the **plug-and-play capability**, we augment both iTransformer (Liu et al., 2024b) and DLinear (Zeng et al., 2023) and further quantify distributional discrepancy using cosine

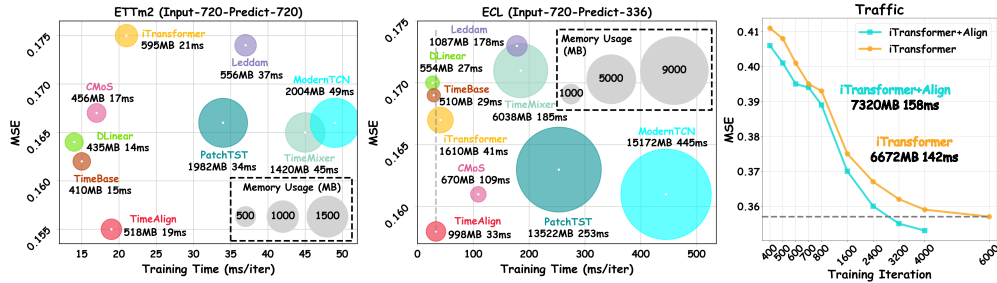


Figure 5: *Left*: Model efficiency comparison under ETTm2 and ECL datasets. *Right*: Training iteration vs. MSE plot. Model training becomes more efficient and effective.

similarity (SIM), and ensure a fair comparison by searching the input length L as Sec. 5.1. As shown in Tab. 3, TimeAlign consistently improves forecasting accuracy by 1%–4% across most benchmarks, while increasing cosine similarity between predictions and ground truth. This dual benefit of low error and high distributional similarity enhances forecast reliability. Performance dips on Weather and Solar datasets are caused by extreme outliers and zero-imputed values, which distort the learned distribution, inflate alignment loss and impair local alignment, respectively. Moreover, these excessively complex architectures hinder the alignment module from effectively correcting the hierarchically extracted representations, leading to inferior performance compared to TimeAlign.

Furthermore, Fig. 5 (right) visualizes the training trajectories of the vanilla and TimeAlign-augmented iTransformer. With the plug-in, TimeAlign guides the encoder towards distributionally coherent minima, slightly increasing GPU memory usage, preserving the original per-iteration latency, and greatly accelerating convergence. On the Traffic dataset, the augmented one reaches the same validation loss 3,000 iterations earlier than the vanilla iTransformer.

5.5 ANALYSIS OF DISTRIBUTION-AWARE ALIGNMENT

Fig. 4 presents t-SNE visualizations of the distributions of the history \mathbf{X} , ground truth \mathbf{Y} , and forecasts from various methods on ECL, Traffic, and ETTm1. (a) \mathbf{X} and \mathbf{Y} exhibit a clear distribution shift with partial overlap. (b) Our $\hat{\mathbf{Y}}_{\text{pred}}$ bridge this gap, matching \mathbf{Y} 's range and fine-grained structure, including peripheral outlier clusters, highlighting the effectiveness of TimeAlign. (c) and (d) contrast the vanilla and TimeAlign-augmented iTransformer and DLinear, respectively.

Furthermore, we categorize the discrepancies between $\hat{\mathbf{Y}}$ and \mathbf{Y} into three patterns. (i) Distribution Mismatch: $\hat{\mathbf{Y}}$ resembles \mathbf{X} more than \mathbf{Y} ; (ii) Distribution Calibration: global shapes align but local modes diverge; (iii) Distribution Absence: $\hat{\mathbf{Y}}$ misses some modes of \mathbf{Y} . Incorporating TimeAlign markedly reduces all three artifacts. On ECL, DLinear's forecasts shift from \mathbf{X} 's skew to \mathbf{Y} 's manifold; on Traffic, both iTransformer's and DLinear's predictions recenter around \mathbf{Y} 's true mean; on ETTm1, absent regions are recovered, yielding almost identical distributions of \mathbf{Y} . These qualitative results confirm TimeAlign is a robust plug-in for distribution alignment across backbones.

5.6 EFFECTIVENESS AND EFFICIENCY

Another key advantage of TimeAlign lies in its **competitive efficiency**, delivering superior performance with few time cost. Using official configurations and the same batch size, Fig. 5 shows that as a purely Linear architecture, TimeAlign surpasses all Transformer- and CNN-based methods in both speed and memory usage, while achieving SOTA training times among Linear-based models.

6 CONCLUSION

This paper introduces TimeAlign, a distribution-aware alignment framework for time series forecasting. By coupling prediction and reconstruction with global and local alignment, TimeAlign effectively bridges the gap between past and future, preserving critical frequency components and boosting forecasting accuracy. Theoretical evidence demonstrates that reconstruction improves forecasting generalization, while alignment increases the mutual information between learned representations and predicted targets. Extensive experiments validate the effectiveness of TimeAlign across diverse benchmarks. We believe that our findings open up promising avenues for reconsidering representation learning in time series forecasting.

7 ETHICS STATEMENT

As our work only focuses on the time series forecasting problem, there is no potential ethical risk.

8 REPRODUCIBILITY STATEMENT

In the main text, we have formally defined the model architecture with equations. All the implementation details, including dataset descriptions, metrics, and experiment configurations, are provided in the manuscript.

ACKNOWLEDGMENTS

This work was supported by DAMO Academy through DAMO Academy Research Intern Program.

REFERENCES

- Alexander A Alemi, Ian Fischer, Joshua V Dillon, and Kevin Murphy. Deep variational information bottleneck. *arXiv preprint arXiv:1612.00410*, 2016.
- Wanlin Cai, Yuxuan Liang, Xianggen Liu, Jianshuai Feng, and Yuankai Wu. Msgnet: Learning multi-scale inter-series correlations for multivariate time series forecasting. *Proceedings of the AAAI Conference on Artificial Intelligence*, 2024.
- Xinlei Chen and Kaiming He. Exploring simple siamese representation learning. In *Proceedings of the IEEE/CVF Conference on Computer Vision and Pattern Recognition (CVPR)*, pp. 15750–15758, June 2021.
- MinGyu Choi and Changhee Lee. Conditional information bottleneck approach for time series imputation. In *The Twelfth International Conference on Learning Representations*, 2023.
- Tao Dai, Beiliang Wu, Peiyuan Liu, Naiqi Li, Jigang Bao, Yong Jiang, and Shu-Tao Xia. Periodicity decoupling framework for long-term series forecasting. *International Conference on Learning Representations*, 2024a.
- Tao Dai, Beiliang Wu, Peiyuan Liu, Naiqi Li, Xue Yuerong, Shu-Tao Xia, and Zexuan Zhu. DDN: Dual-domain dynamic normalization for non-stationary time series forecasting. In *The Thirty-eighth Annual Conference on Neural Information Processing Systems*, 2024b. URL <https://openreview.net/forum?id=RVZfra6sZo>.
- Sijun Dong, Libo Wang, Bo Du, and Xiaoliang Meng. Changeclip: Remote sensing change detection with multimodal vision-language representation learning. *ISPRS Journal of Photogrammetry and Remote Sensing*, 208:53–69, 2024.
- Luo Donghao and Wang Xue. ModernTCN: A modern pure convolution structure for general time series analysis. *International Conference on Learning Representations*, 2024.
- Emadeldeen Eldele, Mohamed Ragab, Zhenghua Chen, Min Wu, and Xiaoli Li. Tslanet: Re-thinking transformers for time series representation learning. In *ICML*, 2024. URL <https://openreview.net/forum?id=CGR3vpX63X>.
- Wei Fan, Pengyang Wang, Dongkun Wang, Dongjie Wang, Yuanchun Zhou, and Yanjie Fu. Dish-TS: a general paradigm for alleviating distribution shift in time series forecasting. In *Proceedings of the AAAI Conference on Artificial Intelligence*, volume 37, pp. 7522–7529, 2023.
- Kaiming He, Haoqi Fan, Yuxin Wu, Saining Xie, and Ross Girshick. Momentum contrast for unsupervised visual representation learning. In *Proceedings of the IEEE/CVF conference on computer vision and pattern recognition*, pp. 9729–9738, 2020.
- Yifan Hu, Yuante Li, Peiyuan Liu, Yuxia Zhu, Naiqi Li, Tao Dai, Shu tao Xia, Dawei Cheng, and Changjun Jiang. Fintsb: A comprehensive and practical benchmark for financial time series forecasting. *arXiv preprint arXiv:2502.18834*, 2025a.

- Yifan Hu, Peiyuan Liu, Yuante Li, Dawei Cheng, Naiqi Li, Tao Dai, Jigang Bao, and Xia Shu-Tao. Finmamba: Market-aware graph enhanced multi-level mamba for stock movement prediction. *arXiv preprint arXiv:2502.06707*, 2025b.
- Yifan Hu, Peiyuan Liu, Peng Zhu, Dawei Cheng, and Tao Dai. Adaptive multi-scale decomposition framework for time series forecasting. In *Proceedings of the AAAI Conference on Artificial Intelligence*, volume 39, pp. 17359–17367, 2025c.
- Yifan Hu, Guibin Zhang, Peiyuan Liu, Disen Lan, Naiqi Li, Dawei Cheng, Tao Dai, Shu-Tao Xia, and Shirui Pan. Timefilter: Patch-specific spatial-temporal graph filtration for time series forecasting. In *Forty-second International Conference on Machine Learning*, 2025d. URL <https://openreview.net/forum?id=490VcNtjh7>.
- Qihe Huang, Zhengyang Zhou, Kuo Yang, Zhongchao Yi, Xu Wang, and Yang Wang. Timebase: The power of minimalism in efficient long-term time series forecasting. In *Forty-second International Conference on Machine Learning*, 2025. URL <https://openreview.net/forum?id=GhTdNOMfOD>.
- Dengyang Jiang, Mengmeng Wang, Liuzhuozheng Li, Lei Zhang, Haoyu Wang, Wei Wei, Guang Dai, Yanning Zhang, and Jingdong Wang. No other representation component is needed: Diffusion transformers can provide representation guidance by themselves. *arXiv preprint arXiv:2505.02831*, 2025.
- Taesung Kim, Jinhee Kim, Yunwon Tae, Cheonbok Park, Jang-Ho Choi, and Jaegul Choo. Reversible instance normalization for accurate time-series forecasting against distribution shift. In *International Conference on Learning Representations*, 2022.
- Diederik P Kingma. Adam: A method for stochastic optimization. *arXiv preprint arXiv:1412.6980*, 2014.
- Xingjian Leng, Jaskirat Singh, Yunzhong Hou, Zhenchang Xing, Saining Xie, and Liang Zheng. Repa-e: Unlocking vae for end-to-end tuning with latent diffusion transformers. *arXiv preprint arXiv:2504.10483*, 2025.
- Chenghan Li, Mingchen Li, and Ruisheng Diao. TVNet: A novel time series analysis method based on dynamic convolution and 3d-variation. In *The Thirteenth International Conference on Learning Representations*, 2025. URL <https://openreview.net/forum?id=MZDdTzN6Cy>.
- Jiexi Liu and Songcan Chen. Timesurl: Self-supervised contrastive learning for universal time series representation learning. *Proceedings of the AAAI Conference on Artificial Intelligence*, 38, 2024. doi: 10.1609/aaai.v38i12.29299. URL <https://ojs.aaai.org/index.php/AAAI/article/view/29299>.
- Peiyuan Liu, Tian Zhou, Liang Sun, and Rong Jin. Mitigating time discretization challenges with weatherode: A sandwich physics-driven neural ode for weather forecasting. *arXiv preprint arXiv:2410.06560*, 2024a.
- Peiyuan Liu, Beiliang Wu, Yifan Hu, Naiqi Li, Tao Dai, Jigang Bao, and Shu-Tao Xia. Timebridge: Non-stationarity matters for long-term time series forecasting. In *Forty-second International Conference on Machine Learning*, 2025. URL <https://openreview.net/forum?id=pyK00ZZ5lz>.
- Yong Liu, Tengge Hu, Haoran Zhang, Haixu Wu, Shiyu Wang, Lintao Ma, and Mingsheng Long. iTransformer: Inverted transformers are effective for time series forecasting. *International Conference on Learning Representations*, 2024b.
- Zhiding Liu, Mingyue Cheng, Zhi Li, Zhenya Huang, Qi Liu, Yanhu Xie, and Enhong Chen. Adaptive normalization for non-stationary time series forecasting: A temporal slice perspective. *Advances in Neural Information Processing Systems*, 36, 2023a.
- Zhiyuan Liu, Yankai Lin, and Maosong Sun. *Representation learning for natural language processing*. Springer Nature, 2023b.

- Hao Miao, Yan Zhao, Chenjuan Guo, Bin Yang, Kai Zheng, Feiteng Huang, Jiandong Xie, and Christian S Jensen. A unified replay-based continuous learning framework for spatio-temporal prediction on streaming data. In *ICDE*, pp. 1050–1062, 2024.
- Hao Miao, Ronghui Xu, Yan Zhao, Senzhang Wang, Jianxin Wang, Philip S Yu, and Christian S Jensen. A parameter-efficient federated framework for streaming time series anomaly detection via lightweight adaptation. *TMC*, 2025.
- Yuqi Nie, Nam H. Nguyen, Phanwadee Sinthong, and Jayant Kalagnanam. A time series is worth 64 words: Long-term forecasting with transformers. In *International Conference on Learning Representations*, 2023.
- Peisong Niu, Ziqing Ma, Tian Zhou, Weiqi Chen, Lefei Shen, Rong Jin, and Liang Sun. Utilizing strategic pre-training to reduce overfitting: Baguan - a pre-trained weather forecasting model. In *Proceedings of the 31st ACM SIGKDD Conference on Knowledge Discovery and Data Mining V.2*, KDD '25, pp. 2186–2197, New York, NY, USA, 2025. Association for Computing Machinery. ISBN 9798400714542. doi: 10.1145/3711896.3737178. URL <https://doi.org/10.1145/3711896.3737178>.
- Aaron van den Oord, Yazhe Li, and Oriol Vinyals. Representation learning with contrastive predictive coding. *arXiv preprint arXiv:1807.03748*, 2018.
- Adam Paszke, Sam Gross, Francisco Massa, Adam Lerer, James Bradbury, Gregory Chanan, Trevor Killeen, Zeming Lin, Natalia Gimelshein, Luca Antiga, et al. Pytorch: An imperative style, high-performance deep learning library. *Advances in Neural Information Processing Systems*, 32, 2019.
- Xiangfei Qiu, Jilin Hu, Lekui Zhou, Xingjian Wu, Junyang Du, Buang Zhang, Chenjuan Guo, Aoying Zhou, Christian S. Jensen, Zhenli Sheng, and Bin Yang. Tfb: Towards comprehensive and fair benchmarking of time series forecasting methods. In *Proc. VLDB Endow.*, pp. 2363–2377, 2024.
- Xiangfei Qiu, Xingjian Wu, Yan Lin, Chenjuan Guo, Jilin Hu, and Bin Yang. Duet: Dual clustering enhanced multivariate time series forecasting. In *SIGKDD*, pp. 1185–1196, 2025.
- Wanneng Shu, Ken Cai, and Neal Naixue Xiong. A short-term traffic flow prediction model based on an improved gate recurrent unit neural network. *IEEE Transactions on Intelligent Transportation Systems*, 23(9):16654–16665, 2021.
- Haotian Si, Changhua Pei, Jianhui li, Dan Pei, and Gaogang Xie. CMos: Rethinking time series prediction through the lens of chunk-wise spatial correlations. In *Forty-second International Conference on Machine Learning*, 2025. URL <https://openreview.net/forum?id=eyjrms4HHm>.
- Huiqiang Wang, Jian Peng, Feihu Huang, Jince Wang, Junhui Chen, and Yifei Xiao. MICN: Multi-scale local and global context modeling for long-term series forecasting. In *International Conference on Learning Representations*, 2022.
- Shiyu Wang, Haixu Wu, Xiaoming Shi, Tengge Hu, Huakun Luo, Lintao Ma, James Y Zhang, and Jun Zhou. TimeMixer: Decomposable multiscale mixing for time series forecasting. *International Conference on Learning Representations*, 2024.
- Haixu Wu, Jiehui Xu, Jianmin Wang, and Mingsheng Long. Autoformer: Decomposition transformers with auto-correlation for long-term series forecasting. *Advances in Neural Information Processing Systems*, 34:22419–22430, 2021.
- Haixu Wu, Tengge Hu, Yong Liu, Hang Zhou, Jianmin Wang, and Mingsheng Long. TimesNet: Temporal 2d-variation modeling for general time series analysis. In *International Conference on Learning Representations*, 2023.
- Zonghan Wu, Shirui Pan, Guodong Long, Jing Jiang, Xiaojun Chang, and Chengqi Zhang. Connecting the dots: Multivariate time series forecasting with graph neural networks. In *Proceedings of the 26th ACM SIGKDD international conference on knowledge discovery & data mining*, pp. 753–763, 2020.

- Jie Yang, Yifan Hu, Kexin Zhang, Luyang Niu, Philip S Yu, and Kaize Ding. Revisiting multivariate time series forecasting with missing values. *arXiv preprint arXiv:2509.23494*, 2025a.
- Jie Yang, Kexin Zhang, Guibin Zhang, Philip S Yu, and Kaize Ding. Glocal information bottleneck for time series imputation. *arXiv preprint arXiv:2510.04910*, 2025b.
- Jie Yang, Rui Zhang, Ziyang Cheng, Dawei Cheng, Guang Yang, and Bo Wang. Grad: Guided relation diffusion generation for graph augmentation in graph fraud detection. In *Proceedings of the ACM on Web Conference 2025*, pp. 5308–5319, 2025c.
- Jie Yang, Yifan Hu, Yuante Li, Kexin Zhang, Kaize Ding, and Philip S Yu. From observations to states: Latent time series forecasting. *arXiv preprint arXiv:2602.00297*, 2026.
- Jingfeng Yao, Bin Yang, and Xinggong Wang. Reconstruction vs. generation: Taming optimization dilemma in latent diffusion models. In *Proceedings of the Computer Vision and Pattern Recognition Conference*, pp. 15703–15712, 2025.
- Guoqi Yu, Jing Zou, Xiaowei Hu, Angelica I Aviles-Rivero, Jing Qin, and Shujun Wang. Revitalizing multivariate time series forecasting: Learnable decomposition with inter-series dependencies and intra-series variations modeling. In *International Conference on Machine Learning*, 2024.
- Sihyun Yu, Sangkyung Kwak, Huiwon Jang, Jongheon Jeong, Jonathan Huang, Jinwoo Shin, and Saining Xie. Representation alignment for generation: Training diffusion transformers is easier than you think. In *The Thirteenth International Conference on Learning Representations*, 2025. URL <https://openreview.net/forum?id=DJSZGGZYVi>.
- Zhihan Yue, Yujing Wang, Juanyong Duan, Tianmeng Yang, Congrui Huang, Yunhai Tong, and Bixiong Xu. Ts2vec: Towards universal representation of time series. In *Proceedings of the AAAI conference on artificial intelligence*, volume 36, pp. 8980–8987, 2022.
- Ailing Zeng, Muxi Chen, Lei Zhang, and Qiang Xu. Are transformers effective for time series forecasting? In *Proceedings of the AAAI conference on artificial intelligence*, volume 37, pp. 11121–11128, 2023.
- Yunhao Zhang and Junchi Yan. Crossformer: Transformer utilizing cross-dimension dependency for multivariate time series forecasting. In *International Conference on Learning Representations*, 2023.
- Haoyi Zhou, Shanghang Zhang, Jieqi Peng, Shuai Zhang, Jianxin Li, Hui Xiong, and Wancai Zhang. Informer: Beyond efficient transformer for long sequence time-series forecasting. In *Proceedings of the AAAI conference on artificial intelligence*, volume 35, pp. 11106–11115, 2021.
- Tian Zhou, Ziqing Ma, Qingsong Wen, Xue Wang, Liang Sun, and Rong Jin. FEDformer: Frequency enhanced decomposed transformer for long-term series forecasting. In *International Conference on Machine Learning*, pp. 27268–27286. PMLR, 2022.

A LLM USAGE

We used Large Language Models (LLMs) as auxiliary tools to assist with the writing process. They were used solely to polish the language and improve readability, with no influence over the research design, experimental implementation or analysis. We conceived and executed all methodological contributions, experiments, and conclusions independently.

B IMPROVE GENERALIZATION WITH RECONSTRUCTION ERROR MINIMIZATION

In this section, we discuss how the representation derived from the minimization of reconstruction error can be used to improve the generalization error. Let $(x_i, y_i), i = 1, \dots, n$ be the set of training examples, where the **latent** input pattern $x_i \in \mathbb{R}^d$ sampled from an Gaussian distribution $\mathcal{N}(0, I_d)$ and the output vector $y_i = (y_{i,1}, \dots, y_{i,d}) \in \mathbb{R}^d$ is constructed as follows:

$$y_{i,j} = \begin{cases} w^\top x_i & j = 1 \\ \sim \mathcal{N}(0, \sigma^2) & j > 1 \end{cases} \quad (13)$$

We now consider learning a linear regression model to map the input x to output y . It is clear that the optimal solution is given by

$$\mathcal{M}_* = e_1 w^\top \quad (14)$$

The empirical estimator learned from the training examples $\{(x_i, y_i)\}_{i=1}^n$ is given by

$$\mathcal{M}_1^\top = \left(\frac{1}{n} \sum_{i=1}^n x_i x_i^\top \right)^{-1} \frac{1}{n} \sum_{i=1}^n x_i y_i^\top = w e_1^\top + \left(\frac{1}{n} \sum_{i=1}^n x_i x_i^\top \right)^{-1} \frac{1}{n} \sum_{i=1}^n x_i z_i^\top \quad (15)$$

where $z_{i,1} = 0$ and $z_{i,j} = y_{i,j}$ for $j \in [2, \dots, d]$. Using the matrix concentration inequality, we have, with a probability $1 - 2\delta$

$$\left| \frac{1}{n} \sum_{i=1}^n x_i x_i^\top - I \right|_2 \leq \sqrt{\frac{6d}{n} \log \frac{d}{\delta}} := \epsilon_a \quad (16)$$

Since

$$\left| \sum_{i=1}^n z_i x_i^\top \right|^2 \sim \sigma^2 \chi_{n(d-1)}^2 \quad (17)$$

we have, with a probability $1 - \delta$

$$\left| \sum_{i=1}^n z_i x_i^\top \right|_F^2 \geq n(d-1)\sigma^2 \left(1 - \sqrt{\frac{3}{n(d-1)} \log \frac{1}{\delta}} \right) \quad (18)$$

As a result, with a probability at least $1 - 3\delta$, we have

$$\begin{aligned} \frac{|\mathcal{M}_1 - \mathcal{M}_*|}{|\mathcal{M}_*|} &= \frac{1}{|\mathcal{M}_*|} \left| \left(\frac{1}{n} \sum_{i=1}^n x_i x_i^\top \right)^{-1} \frac{1}{n} \sum_{i=1}^n z_i x_i \right| \\ &\geq \frac{\sigma}{|w|} \left(1 + \sqrt{\frac{6d}{n} \log \frac{d}{\delta}} \right)^{-1} \sqrt{\frac{d-1}{n} \left(1 - \sqrt{\frac{3}{n(d-1)} \log \frac{1}{\delta}} \right)} \\ &= \Omega \left(\frac{\sigma}{|w|} \sqrt{\frac{d}{n}} \right) \end{aligned} \quad (19)$$

Our second approach is to first learn one dimension representation for each y_i by minimizing the reconstruction error, and then learn a linear regression model from the derived one dimension representation. The one dimension representation is derived by minimizing the following reconstruction error:

$$\min_{u \in \mathbb{R}^n, v \in \mathbb{R}^d} |Y - vu^\top|_F^2 \quad (20)$$

where $Y = (y_1, \dots, y_n) \in \mathbb{R}^{d \times n}$. Evidently, v and u are the left and right singular vectors of Y with the largest singular value. We first write YY^\top as

$$\frac{1}{n}YY^\top = \left(\frac{1}{n} \sum_{i=1}^n (w^\top x_i)^2 \right) e_1 e_1^\top + \frac{1}{n} \sum_{i=1}^n z_i z_i^\top \quad (21)$$

Using the Davis–Kahan $\sin \theta$ theorem, we have

$$\sin \theta(v, e_1) \leq \frac{\left| \frac{1}{n} \sum_{i=1}^n z_i z_i^\top \right|_2}{\frac{1}{n} \sum_{i=1}^n (w^\top x_i)^2} \quad (22)$$

Using the matrix concentration inequality, we have, with a probability $1 - 2\delta$,

$$\left| \frac{1}{n} \sum_{i=1}^n z_i z_i^\top \right|_2 \leq \sigma^2 \left(1 + \sqrt{\frac{6d}{n} \log \frac{1}{\delta}} \right) \quad (23)$$

Since

$$\sum_{i=1}^n (w^\top x_i)^2 \sim |w|^2 \chi_n^2 \quad (24)$$

we have, with a probability $1 - \delta$

$$\frac{1}{n} \sum_{i=1}^n (w^\top x_i)^2 \geq \left(1 - \sqrt{\frac{3}{n} \log \frac{1}{\delta}} \right) |w|^2 \quad (25)$$

As a result, with a probability at least $1 - 2\delta$,

$$\sin \theta(v, e_1) \leq \frac{\sigma^2}{|w|^2} \frac{1 + \sqrt{\frac{6d}{n} \log \frac{1}{\delta}}}{1 - \sqrt{\frac{3}{n} \log \frac{1}{\delta}}} \quad (26)$$

As a result, the one dimension representation $u = (u_1, \dots, u_n) = Y^\top v$, where each u_i is given by

$$u_i = v^\top y_i = w^\top x_i + (v - e_1)^\top y_i \quad (27)$$

Using the one dimension representation u , we obtain a new estimator \mathcal{M}_2 given by

$$\mathcal{M}_2^\top = \left(\frac{1}{n} \sum_{i=1}^n x_i x_i^\top \right)^{-1} \frac{1}{n} \sum_{i=1}^n x_i u_i v^\top = (v^\top e_1) w v^\top + \left(\frac{1}{n} \sum_{i=1}^n x_i x_i^\top \right)^{-1} \frac{1}{n} \sum_{i=1}^n x_i z_i^\top v v^\top \quad (28)$$

First, we have, with a probability $1 - \delta$

$$\begin{aligned} & |(v^\top e_1) w v^\top - w e_1^\top|_F \leq |1 - v^\top e_1| |w| + |w| |v - e_1| \\ & \leq \left(|1 - \cos \theta(v, e_1)| + \sqrt{\sin^2 \theta(v, e_1) + (1 - \cos \theta(v, e_1))^2} \right) |w| \\ & = \left(|1 - \cos \theta(v, e_1)| + \sqrt{2 - 2 \cos \theta(v, e_1)} \right) |w| = 2 \left(\sin^2 \frac{\theta(v, e_1)}{2} + \sin \frac{\theta(v, e_1)}{2} \right) |w| \quad (29) \\ & \leq 4 \sin \theta(v, e_1) |w| \leq \frac{4\sigma^2}{|w|} \frac{1 + \sqrt{\frac{6d}{n} \log \frac{1}{\delta}}}{1 - \sqrt{\frac{3}{n} \log \frac{1}{\delta}}} \end{aligned}$$

Second, since

$$\left| \frac{1}{n} \sum_{i=1}^n x_i z_i^\top v v^\top \right|_F \leq \left| \frac{1}{n} \sum_{i=1}^n x_i z_i^\top \right|_2 \quad (30)$$

using the matrix concentration inequality, we have, with a probability $1 - 2\delta$,

$$\left| \frac{1}{n} \sum_{i=1}^n z_i x_i^\top \right|_2 \leq \frac{4\sigma}{3n} \log \frac{d}{\delta} \sqrt{\log \frac{n}{\delta}} + \sigma \sqrt{\frac{2}{n} \log \frac{d}{\delta}} \quad (31)$$

Hence, with a probability $1 - 3\delta$, we have

$$\left| \left(\frac{1}{n} \sum_{i=1}^n x_i x_i^\top \right)^{-1} \frac{1}{n} \sum_{i=1}^n x_i z_i^\top v v^\top \right|_F \leq \sigma \left(1 - \sqrt{\frac{6d}{n} \log \frac{d}{\delta}} \right)^{-1} \left(\frac{4}{3n} \log^{3/2} \frac{d}{\delta} + \sqrt{\frac{2}{n} \log \frac{d}{\delta}} \right) \quad (32)$$

Finally, with a probability $1 - 3\delta$, we have

$$\begin{aligned} \frac{|\mathcal{M}_2 - \mathcal{M}_*|_F}{|\mathcal{M}_*|_F} &\leq \frac{\sigma}{|w|} \left\{ \frac{\sigma}{|w|} \frac{1 + \sqrt{\frac{6d}{n} \log \frac{1}{\delta}}}{1 - \sqrt{\frac{3}{n} \log \frac{1}{\delta}}} + \left(1 - \sqrt{\frac{6d}{n} \log \frac{d}{\delta}} \right)^{-1} \left(\frac{4}{3n} \log^{3/2} \frac{d}{\delta} + \sqrt{\frac{2}{n} \log \frac{d}{\delta}} \right) \right\} \\ &= \Omega \left(\frac{\sigma^2}{|w|^2} + \frac{\sigma}{|w|\sqrt{n}} \right) \end{aligned} \quad (33)$$

where $|\cdot|_F$ denotes the Frobenius norm. And when

$$\sigma \ll |w| \sqrt{\frac{d}{n}} \quad (34)$$

we have

$$\frac{|\mathcal{M}_2 - \mathcal{M}_*|_F}{|\mathcal{M}_*|_F} \ll \frac{|\mathcal{M}_1 - \mathcal{M}_*|_F}{|\mathcal{M}_*|_F} \quad (35)$$

Therefore, under the stated assumptions, the reconstruction-based estimator \mathcal{M}_2 achieves a strictly tighter approximation to \mathcal{M}^* than \mathcal{M}_1

C DETAILED DERIVATION OF MUTUAL INFORMATION MAXIMIZATION

This section provides a detailed derivation showing that our proposed method, TimeAlign, is grounded in the principle of Mutual Information Maximization (MIM). We demonstrate that our loss functions, $\mathcal{L}_{\text{pred}}$ and $\mathcal{L}_{\text{align}}$, are formulated to maximize the mutual information between the representation \mathbf{H}_x and the ground truth \mathbf{Y} .

C.1 DERIVATION OF PREDICTION LOSS $\mathcal{L}_{\text{PRED}}$

Here, we illustrate the entire derivation of the mutual information $I(\mathbf{Y}; \mathbf{H}_x)$ in Eq. 11. We begin by deriving the prediction loss, $\mathcal{L}_{\text{pred}}$. As presented in Eq. 11, this loss is directly related to the mutual information term $I(\mathbf{Y}; \mathbf{H}_x)$. Using variational inference, we establish a lower bound for this term:

$$\begin{aligned} I(\mathbf{Y}; \mathbf{H}_x) &= \mathbb{E}_{p(y, h_x)} \left[\log \frac{p(y, h_x)}{p(y) \cdot p(h_x)} \right], \\ &= \mathbb{E}_{p(y, h_x)} \left[\log \frac{p(y|h_x) \cdot p(h_x)}{p(y) \cdot p(h_x)} \right], \\ &= \mathbb{E}_{p(y, h_x)} \left[\log \frac{p(y|h_x)}{p(y)} \right], \\ &= \mathbb{E}_{p(y, h_x)} \left[\log \frac{p(y|h_x) \cdot \mathcal{F}_\theta(y|h_x)}{p(y) \cdot \mathcal{F}_\theta(y|h_x)} \right], \\ &= \mathbb{E}_{p(y, h_x)} \left[\log \frac{\mathcal{F}_\theta(y|h_x)}{p(y)} \right] + \mathbb{E}_{p(y, h_x)} \left[\log \frac{p(y|h_x)}{\mathcal{F}_\theta(y|h_x)} \right]. \end{aligned} \quad (36)$$

The second term is the Kullback-Leibler (KL) divergence between the true posterior $p(y|h_x)$ and the variational approximation $\mathcal{F}_\theta(y|h_x)$. The equation can thus be rewritten as follows:

$$\begin{aligned} I(\mathbf{Y}; \mathbf{H}_x) &= \mathbb{E}_{p(y, h_x)} \left[\log \frac{\mathcal{F}_\theta(y|h_x)}{p(y)} \right] + \int_{h_x} \int_y p(y, h_x) \cdot \log \frac{p(y|h_x)}{\mathcal{F}_\theta(y|h_x)} dy dh_x, \\ &= \mathbb{E}_{p(y, h_x)} \left[\log \frac{\mathcal{F}_\theta(y|h_x)}{p(y)} \right] + \int_{h_x} \int_y p(y|h_x) \cdot p(h_x) \cdot \log \frac{p(y|h_x)}{\mathcal{F}_\theta(y|h_x)} dy dh_x, \\ &= \mathbb{E}_{p(y, h_x)} \left[\log \frac{\mathcal{F}_\theta(y|h_x)}{p(y)} \right] + \int_{h_x} p(h_x) \cdot D_{\text{KL}}[p(y|h_x) || \mathcal{F}_\theta(y|h_x)] dh_x. \end{aligned} \quad (37)$$

Since the KL divergence term is non-negative ($D_{KL}[\cdot|\cdot] \geq 0$), we can establish a lower bound for the mutual information as follows:

$$\begin{aligned}
I(\mathbf{Y}; \mathbf{H}_x) &= \mathbb{E}_{p(y, h_x)} \left[\log \frac{\mathcal{F}_\theta(y|h_x)}{p(y)} \right] + \int_{h_x} p(h_x) \cdot D_{KL}[p(y|h_x) || \mathcal{F}_\theta(y|h_x)] dh_x, \\
&\geq \mathbb{E}_{p(y, h_x)} \left[\log \frac{\mathcal{F}_\theta(y|h_x)}{p(y)} \right], \\
&= \mathbb{E}_{p(y, h_x)} [\log \mathcal{F}_\theta(y|h_x)] - \mathbb{E}_{p(y, h_x)} [\log p(y)], \\
&\geq \mathbb{E}_{p(y, h_x)} [\log \mathcal{F}_\theta(y|h_x)] \stackrel{\text{def}}{=} -\mathcal{L}_{\text{pred}}.
\end{aligned} \tag{38}$$

As we assume that prediction errors follow a Laplace distribution with fixed scale parameter b :

$$y = \hat{y} + \epsilon, \quad \text{where } \epsilon \sim \left(\frac{1}{2b} \right)^T \exp \left(-\frac{\|\epsilon - 0\|_1}{b} \right). \tag{39}$$

Therefore, $\mathcal{F}_\theta(y|h_x) = \left(\frac{1}{2b} \right)^T \exp \left(-\frac{\|y - \hat{y}\|_1}{b} \right)$. The derived prediction loss can be further simplified to the form of MAE loss:

$$\mathcal{L}_{\text{pred}} = -\mathbb{E}_{p(y, h_x)} \left[-T \log(2b) - \frac{1}{b} \|y - \hat{y}\|_1 \right] \propto \mathbb{E}_{p(y, h_x)} [\|y - \hat{y}\|_1], \tag{40}$$

where \hat{y} denotes the predict results generated by the model, and T is the forecasting horizon.

C.2 DERIVATION OF ALIGNMENT LOSS $\mathcal{L}_{\text{ALIGN}}$

In addition to the prediction loss, we introduce an alignment loss, $\mathcal{L}_{\text{align}}$, to further maximize the mutual information between the representation \mathbf{H}_x and the ground truth \mathbf{Y} . Inspired by contrastive learning, we derive an alternative lower bound for $I(\mathbf{Y}; \mathbf{H}_x)$ based on the InfoNCE objective (Oord et al., 2018):

$$\begin{aligned}
I(\mathbf{Y}; \mathbf{H}_x) &= \mathbb{E}_{p(y, h_x)} \left[\log \left(\frac{p(y, h_x)}{p(y) \cdot p(h_x)} \right) \right], \\
&= \mathbb{E}_{p(y, h_x)} \left[\log \left(\frac{p(y|h_x) \cdot p(h_x)}{p(y) \cdot p(h_x)} \right) \right], \\
&= \mathbb{E}_{p(y, h_x)} \left[\log \left(\frac{p(y|h_x)}{p(y)} \right) \right], \\
&= -\mathbb{E}_{p(y, h_x)} \left[\log \left(\frac{p(y)}{p(y|h_x)} \right) \right], \\
&= -\mathbb{E}_{p(y, h_x)} \left[\log \left(\frac{p(y)}{p(y|h_x)} \cdot N \right) - \log N \right], \\
&\approx -\mathbb{E}_{p(y, h_x)} \left[\log \left(\frac{p(y)}{p(y|h_x)} \cdot N \right) \right], \\
&\geq -\mathbb{E}_{p(y, h_x)} \left[\log \left(1 + \frac{p(y)}{p(y|h_x)} \cdot (N-1) \cdot 1 \right) \right], \\
&= -\mathbb{E}_{p(y, h_x)} \left[\log \left(1 + \frac{p(y)}{p(y|h_x)} \cdot (N-1) \cdot \mathbb{E}_{p(y_j)} \left(\frac{p(y_j|h_x)}{p(y_j)} \right) \right) \right], \\
&= \mathbb{E}_{p(y, h_x)} \left[\log \left(\frac{\frac{p(y|h_x)}{p(y)}}{\frac{p(y|h_x)}{p(y)} + \sum_{y_j \in \mathbf{Y}^{\text{neg}}} \frac{p(y_j|h_x)}{p(y_j)}} \right) \right], \\
&= \mathbb{E}_{p(y, h_x)} \left[\log \left(\frac{f(y, h_x)}{f(y, h_x) + \sum_{y_j \in \mathbf{Y}^{\text{neg}}} f(y_j, h_x)} \right) \right].
\end{aligned} \tag{41}$$

Here, $f(y, h_x) = \exp(\text{proj}(h_x)^\top \cdot \mathcal{G}_\phi(y))$ is a density ratio that is proportional to $\frac{p(y|h_x)}{p(y)}$. Following common practice (Choi & Lee, 2023), we use an in-batch negative sampling strategy, where negative samples are drawn from other instances in the same mini-batch.

Furthermore, inspired by recent advances in contrastive learning (He et al., 2020; Chen & He, 2021), we simplify Eq. 41 as follows:

$$\begin{aligned} I(\mathbf{Y}; \mathbf{H}_x) &\approx -\mathbb{E}_{p(y, h_x)} [f(y, h_x)], \\ &= -\mathbb{E}_{p(y, h_x)} [\exp(\text{proj}(h_x)^\top \cdot \mathcal{G}_\phi(y))] \stackrel{\text{def}}{=} -\mathcal{L}_{\text{align}}. \end{aligned} \quad (42)$$

Therefore, we get a simpler alignment loss in Eq. 12, which further enhances the mutual information between the representation \mathbf{H}_x and the ground truth \mathbf{Y} .

D EXPERIMENT DETAILS

D.1 METRIC DETAILS

We use Mean Squared Error (MSE) and Mean Absolute Error (MAE) as evaluation metrics. Given the ground truth values \mathbf{Y}_i and the predicted values $\hat{\mathbf{Y}}_i$, these metrics are defined as follows:

$$\text{MSE} = \frac{1}{N} \sum_{i=1}^N (\mathbf{Y}_i - \hat{\mathbf{Y}}_i)^2, \quad \text{MAE} = \frac{1}{N} \sum_{i=1}^N |\mathbf{Y}_i - \hat{\mathbf{Y}}_i| \quad (43)$$

where N is the total number of predictions.

D.2 DATASETS

Time series forecasting is a fundamental problem with a wide range of applications in areas such as climate modeling (Niu et al., 2025; Liu et al., 2024a), finance analysis (Hu et al., 2025a;b), traffic flow prediction (Shu et al., 2021; Miao et al., 2024; Qiu et al., 2025) and so on. From these areas, we choose several widely-used time series datasets and conduct extensive experiments on TSF. We report the statistics in Tab. 4. Detailed descriptions of these datasets are as follows:

- (1) **ETT** (Electricity Transformer Temperature) dataset (Zhou et al., 2021) encompasses temperature and power load data from electricity transformers in two regions of China, spanning from 2016 to 2018. This dataset has two granularity levels: ETTh (hourly) and ETTm (15 minutes).
- (2) **Weather** dataset (Wu et al., 2023) captures 21 distinct meteorological indicators in Germany, meticulously recorded at 10-minute intervals throughout 2020. Key indicators in this dataset include air temperature, visibility, among others, offering a comprehensive view of the weather dynamics.
- (3) **Electricity** dataset (Wu et al., 2023) features hourly electricity consumption records in kilowatt-hours (kWh) for 321 clients. Sourced from the UCL Machine Learning Repository, this dataset covers the period from 2012 to 2014, providing valuable insights into consumer electricity usage patterns.
- (4) **Traffic** dataset (Wu et al., 2023) includes data on hourly road occupancy rates, gathered by 862 detectors across the freeways of the San Francisco Bay area. This dataset, covering the years 2015 to 2016, offers a detailed snapshot of traffic flow and congestion.
- (5) **Solar-Energy** dataset (Liu et al., 2024b) contains solar power production data recorded every 10 minutes throughout 2006 from 137 photovoltaic (PV) plants in Alabama.

D.3 IMPLEMENTATION DETAILS

All experiments are implemented in PyTorch (Paszke et al., 2019) and conducted on one NVIDIA V100 32GB GPU. We use the Adam optimizer (Kingma, 2014) with a learning rate selected from $\{1e^{-3}, 5e^{-4}, 1e^{-4}\}$. The batch size is set to 16 for the Electricity and Traffic datasets, and 32 for all other datasets. Tab. 5 provides detailed hyperparameter settings for each dataset.

Dataset	Dim	Prediction Length	Dataset Size	Frequency
ETTm1	7	{96, 192, 336, 720}	(34465, 11521, 11521)	15 min
ETTm2	7	{96, 192, 336, 720}	(34465, 11521, 11521)	15 min
ETTh1	7	{96, 192, 336, 720}	(8545, 2881, 2881)	1 hour
ETTh2	7	{96, 192, 336, 720}	(8545, 2881, 2881)	1 hour
Electricity	321	{96, 192, 336, 720}	(18317, 2633, 5261)	1 hour
Traffic	862	{96, 192, 336, 720}	(12185, 1757, 3509)	1 hour
Weather	21	{96, 192, 336, 720}	(36792, 5271, 10540)	10 min
Solar-Energy	137	{96, 192, 336, 720}	(36601, 5161, 10417)	10 min

Table 4: Dataset detailed descriptions. “Dataset Size” denotes the total number of time points in (Train, Validation, Test) split respectively. “Prediction Length” denotes the future time points to be predicted. “Frequency” denotes the sampling interval of time points.

Tasks	Dataset	e_layers	lr	d_model	d_ff	Num. of Patches	Num. of Epochs
Long-term Forecasting	ETTm1	2	1e-4	128	256	1	10
	ETTm2	2	1e-4	128	128	12	10
	ETTh1	2	5e-4	32	32	24	10
	ETTh2	2	5e-4	32	32	48	10
	Weather	2	1e-4	128	256	48	10
	Electricity	2	5e-4	512	2048	1	10
	Traffic	2	1e-3	512	2048	1	30
	Solar-Energy	2	5e-4	256	256	1	10

Table 5: Hyperparameter settings for different datasets. “e_layers” denotes the number of graph block. “lr” denotes the learning rate. “d_model” and “d_ff” denote the model dimension of attention layers and feed-forward layers, respectively.

E FULL RESULTS

E.1 MAIN EXPERIMENTS

Tab. 6 and Fig. 6 present the full results for long-term forecasting, where the results are obtained through hyperparameter search. The look-back horizons is searched from {192, 336, 512, 720}. TimeAlign consistently achieves the best performance, demonstrating its effectiveness and robustness.

E.2 ERROR BARS

In this paper, we repeat all the experiments three times. Here we report the standard deviation of our proposed TimeAlign and the second best model TVNet (Li et al., 2025), as well as the statistical significance test in Tab. 7. We perform the Wilcoxon test with TVNet (Li et al., 2025) and obtain the p-value of $1.37e^{-8}$, indicating a significant improvement at the 99% confidence level.

E.3 ABLATION STUDIES

Tab. 8 presents the full results of the ablation studies discussed in the main text. ① **w/o Align** signifies the

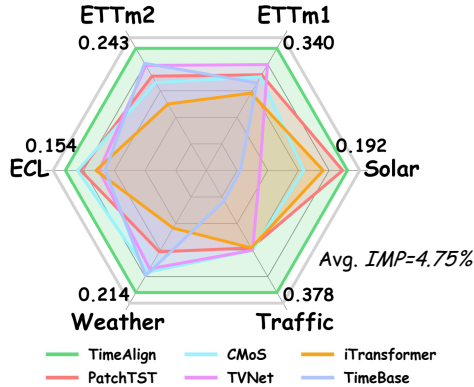


Figure 6: MSE Performance of TimeAlign.

Predict Branch alone, with both Local and Global

Alignment removed. ② **w/ Local only** denotes the Local Alignment module is retained to refine point-to-point similarity, while Global Alignment is disabled. ③ **w/ Global only** denotes only the Global Alignment is retained to coarsely align the embedding distributions, while Local Alignment is omitted. ④ **w/ Align** encompasses both Local and Global Alignment mechanisms.

E.4 PLUG-AND-PLAY EXPERIMENT

Tab. 9 presents the full results for Plug-and-Play experiment. TimeAlign enhances forecasting accuracy across diverse benchmarks while improving alignment between predicted and ground-truth sequences in the representation space. This combined improvement in predictive precision and distributional consistency results in more reliable forecasts.

E.5 EXTRA ANALYSIS OF RECONSTRUCTION

To validate the effect of reconstruction, we visualize the patch-wise similarity of history, ground truth, reconstructed series, and forecasts with and without alignment on the ETTm1, ECL, and

Models	TimeAlign (Ours)		CMoS (2025)		TimeBase (2025)		TVNet (2025)		iTransformer (2024b)		TimeMixer (2024)		Leddam (2024)		ModernTCN (2024)		PatchTST (2023)		Crossformer (2023)		TimesNet (2023)		DLinear (2023)		
	MSE	MAE	MSE	MAE	MSE	MAE	MSE	MAE	MSE	MAE	MSE	MAE	MSE	MAE	MSE	MAE	MSE	MAE	MSE	MAE	MSE	MAE	MSE	MAE	
ETTM1	96	0.279	0.330	0.292	0.345	0.311	0.351	<u>0.288</u>	<u>0.343</u>	0.300	0.353	0.293	0.345	0.294	0.347	0.292	0.346	0.293	0.346	0.310	0.361	0.338	0.375	0.300	0.345
	192	0.322	0.356	0.334	<u>0.366</u>	0.338	0.371	<u>0.326</u>	<u>0.367</u>	0.345	0.382	0.335	0.372	0.334	0.370	0.332	0.368	0.333	0.370	0.363	0.402	0.371	0.387	0.336	<u>0.366</u>
	336	0.350	0.375	0.366	<u>0.386</u>	<u>0.364</u>	<u>0.386</u>	0.365	0.391	0.374	0.398	0.368	<u>0.386</u>	0.392	0.425	0.365	0.391	0.369	0.369	0.389	0.430	0.410	0.411	0.367	<u>0.386</u>
	720	0.407	0.406	0.425	0.417	0.413	0.414	<u>0.412</u>	<u>0.413</u>	0.429	0.430	0.426	0.417	0.421	0.419	0.416	0.417	0.416	0.420	0.600	0.547	0.478	0.450	0.419	0.416
	Avg.	0.340	0.367	0.354	<u>0.378</u>	0.357	0.380	<u>0.348</u>	<u>0.379</u>	0.362	0.391	0.355	0.380	0.354	0.381	0.351	0.381	0.353	0.382	0.420	0.435	0.400	0.406	0.356	<u>0.378</u>
ETTM2	96	0.155	0.241	0.167	0.257	0.162	0.256	<u>0.161</u>	<u>0.254</u>	0.175	0.266	0.165	0.256	0.174	0.260	0.166	0.256	0.166	0.256	0.263	0.359	0.189	0.265	0.164	0.255
	192	0.210	0.280	0.228	0.299	<u>0.218</u>	<u>0.293</u>	0.220	<u>0.293</u>	0.242	0.312	0.225	0.298	0.231	0.301	0.222	<u>0.293</u>	0.223	0.296	0.345	0.400	0.254	0.310	0.224	0.304
	336	0.263	0.315	0.273	0.325	<u>0.270</u>	<u>0.328</u>	0.272	<u>0.316</u>	0.282	0.340	0.277	0.332	0.288	0.336	0.272	0.324	0.274	0.329	0.469	0.496	0.313	0.345	0.277	0.337
	720	0.343	0.372	0.367	0.385	0.352	0.380	<u>0.349</u>	<u>0.379</u>	0.378	0.398	0.360	0.387	0.368	0.386	0.351	0.381	0.362	0.385	0.996	0.750	0.413	0.402	0.371	0.401
	Avg.	0.243	0.302	0.259	0.316	<u>0.250</u>	0.314	0.251	<u>0.311</u>	0.269	0.329	0.257	0.318	0.265	0.320	0.253	0.314	0.256	0.317	0.518	0.501	0.292	0.330	0.259	0.324
ETTh1	96	0.362	0.387	<u>0.361</u>	0.383	0.349	<u>0.384</u>	0.371	0.408	0.386	0.405	0.372	0.401	0.377	0.394	0.368	0.394	0.377	0.397	0.386	0.426	0.384	0.402	0.379	0.403
	192	0.404	0.412	0.405	0.409	0.387	<u>0.410</u>	<u>0.398</u>	0.409	0.424	0.440	0.413	0.430	0.408	0.427	0.405	0.413	0.409	0.428	0.413	0.442	0.557	0.436	0.408	0.419
	336	0.424	0.430	0.412	0.420	0.408	0.418	<u>0.401</u>	0.409	0.449	0.460	0.438	0.450	0.424	0.437	0.391	<u>0.412</u>	0.431	0.444	0.440	0.461	0.491	0.469	0.440	0.440
	720	0.433	<u>0.451</u>	0.433	<u>0.451</u>	<u>0.439</u>	0.446	0.458	0.459	0.495	0.487	0.486	0.484	0.451	0.465	0.450	0.461	0.457	0.477	0.519	0.524	0.521	0.500	0.471	0.493
	Avg.	0.406	0.420	<u>0.403</u>	<u>0.416</u>	0.396	0.414	0.407	0.421	0.439	0.448	0.427	0.441	0.415	0.430	0.404	0.420	0.418	0.436	0.440	0.463	0.458	0.450	0.424	0.439
ETTM2	96	<u>0.266</u>	0.328	0.274	0.341	0.292	0.345	<u>0.263</u>	<u>0.329</u>	0.297	0.348	0.281	0.351	0.283	0.345	<u>0.263</u>	0.332	0.274	0.337	0.611	0.557	0.334	0.370	0.289	0.353
	192	0.330	0.372	0.333	0.383	0.339	0.387	0.319	0.372	0.371	0.403	0.349	0.387	0.339	0.381	<u>0.320</u>	<u>0.374</u>	0.348	0.384	0.703	0.624	0.404	0.413	0.383	0.418
	336	0.360	0.399	0.342	0.384	0.358	0.410	0.311	0.373	0.404	0.428	0.366	0.413	0.366	0.405	<u>0.313</u>	<u>0.376</u>	0.377	0.416	0.827	0.675	0.389	0.435	0.448	0.465
	720	<u>0.388</u>	<u>0.428</u>	0.374	0.423	0.400	0.448	0.401	0.434	0.424	0.444	0.401	0.436	0.395	0.436	0.392	0.433	0.406	0.441	1.094	0.775	0.434	0.448	0.605	0.551
	Avg.	0.336	0.382	0.331	0.383	0.345	0.397	<u>0.324</u>	0.377	0.374	0.406	0.349	0.397	0.345	0.391	0.322	<u>0.379</u>	0.351	0.404	0.809	0.658	0.390	0.427	0.431	0.447
Weather	96	0.140	0.179	<u>0.144</u>	<u>0.193</u>	0.146	0.198	0.147	0.198	0.159	0.208	0.147	0.198	0.149	0.200	0.149	0.200	0.149	0.198	0.146	0.212	0.172	0.220	0.170	0.230
	192	0.182	0.220	0.186	<u>0.237</u>	<u>0.185</u>	0.241	0.194	0.238	0.200	0.248	0.192	0.243	0.193	0.240	0.196	0.245	0.194	0.241	0.195	0.261	0.219	0.261	0.216	0.273
	336	0.232	0.262	0.240	0.281	0.236	0.281	<u>0.235</u>	<u>0.277</u>	0.253	0.289	0.247	0.284	0.241	0.279	0.238	<u>0.277</u>	0.245	0.282	0.252	0.311	0.280	0.306	0.258	0.307
	720	0.307	0.317	0.311	0.332	0.309	0.331	<u>0.308</u>	0.331	0.321	0.338	0.318	<u>0.330</u>	0.324	0.338	0.314	0.334	0.314	0.334	0.318	0.363	0.365	0.359	0.323	0.362
	Avg.	0.214	0.244	0.220	<u>0.261</u>	<u>0.219</u>	0.263	0.221	<u>0.261</u>	0.233	0.271	0.226	0.264	0.226	0.264	0.224	0.264	0.226	0.264	0.228	0.287	0.259	0.287	0.242	0.293
Electricity	96	<u>0.126</u>	0.216	<u>0.129</u>	0.223	0.139	0.231	0.142	0.223	0.138	0.237	0.142	0.247	0.134	0.228	<u>0.129</u>	0.226	<u>0.129</u>	<u>0.222</u>	0.135	0.237	0.168	0.272	0.140	0.237
	192	<u>0.143</u>	0.233	<u>0.142</u>	<u>0.236</u>	0.153	0.245	0.165	0.241	0.157	0.256	0.168	0.269	0.155	0.248	<u>0.143</u>	0.239	0.147	0.240	0.160	0.262	0.184	0.289	0.152	0.249
	336	0.158	0.249	<u>0.161</u>	<u>0.254</u>	0.169	0.262	0.164	0.269	0.167	0.264	0.171	0.260	0.173	0.268	<u>0.161</u>	0.259	0.163	0.259	0.182	0.282	0.198	0.300	0.170	0.267
	720	<u>0.189</u>	0.278	0.200	0.288	0.207	0.294	0.190	0.284	0.194	0.286	0.209	0.313	0.186	<u>0.282</u>	0.191	0.286	0.197	0.290	0.246	0.337	0.220	0.320	0.203	0.301
	Avg.	0.154	0.244	0.158	<u>0.250</u>	0.167	0.258	0.165	0.254	0.164	0.261	0.185	0.284	0.162	0.256	<u>0.156</u>	0.253	0.159	0.253	0.181	0.279	0.192	0.295	0.166	0.264
Traffic	96	0.349	0.225	0.367	0.256	0.394	0.267	0.367	<u>0.252</u>	<u>0.363</u>	0.265	0.369	0.257	0.415	0.264	0.368	0.253	0.370	0.262	0.512	0.282	0.593	0.321	0.395	0.275
	192	0.365	0.233	<u>0.379</u>	<u>0.261</u>	0.403	0.271	0.381	0.262	0.385	0.273	0.400	0.272	0.445	0.277	<u>0.379</u>	<u>0.261</u>	0.386	0.269	0.501	0.273	0.617	0.336	0.407	0.280
	336	0.377	0.240	0.397	0.270	0.417	0.278	<u>0.395</u>	<u>0.268</u>	0.396	0.277	0.407	0.272	0.461	0.286	0.397	0.270	0.396	0.275	0.507	0.279	0.629	0.336	0.417	0.286
	720	0.422	0.263	0.442	0.295	0.456	0.298	0.442	<u>0.290</u>	0.445	0.308	0.461	0.316	0.489	0.305	0.440	0.296	<u>0.435</u>	0.295	0.571	0.301	0.640	0.350	0.454	0.308
	Avg.	0.378	0.240	<u>0.396</u>	<u>0.270</u>	0.417	0.278	<u>0.396</u>	<u>0.268</u>	0.397	0.282	0.409	0.279	0.452	0.283	<u>0.396</u>	0.270	0.397	0.275	0.523	0.284	0.620	0.336	0.418	0.287
Solar	96	0.172	0.200	0.188	0.241	0.220	0.269	0.204	0.260	0.188	0.232	0.179	0.232	0.197	0.241	0.202	0.263	<u>0.178</u>	0.229	0.183	<u>0.208</u>	0.219	0.314	0.197	0.210
	192	0.189	0.213	0.207	0.256	0.232	0.266	0.227	0.272	<u>0.193</u>	0.248	0.201	0.259	0.231	0.264	0.223	0.279	0.189	0.246	0.208	<u>0.226</u>	0.231	0.322	0.218	0.222
	336	0.204	0.219	0.219	0.263	0.247	0.274	0.241	0.288	0.203	0.249	0.190	0.256	0.216	0.272	0.241	0.292	<u>0.198</u>	0.249	0.212	<u>0.239</u>	0.246	0.337	0.234	0.231
	720	0.202	0.224</																						

Model	TimeAlign		TVNet (2025)		Confidence
Dataset	MSE	MAE	MSE	MAE	Interval
ETTm1	0.340 ± 0.011	0.367 ± 0.008	0.348 ± 0.009	0.379 ± 0.007	99%
ETTm2	0.243 ± 0.006	0.302 ± 0.006	0.250 ± 0.004	0.311 ± 0.005	99%
ETTh1	0.406 ± 0.009	0.420 ± 0.007	0.407 ± 0.010	0.421 ± 0.009	99%
ETTh2	0.336 ± 0.014	0.382 ± 0.012	0.324 ± 0.011	0.377 ± 0.015	99%
Weather	0.214 ± 0.009	0.244 ± 0.007	0.221 ± 0.008	0.261 ± 0.008	99%
Electricity	0.154 ± 0.013	0.244 ± 0.008	0.165 ± 0.008	0.254 ± 0.006	99%
Traffic	0.378 ± 0.010	0.240 ± 0.011	0.396 ± 0.010	0.268 ± 0.013	99%
Solar	0.192 ± 0.012	0.214 ± 0.013	0.228 ± 0.011	0.277 ± 0.009	99%

Table 7: Standard deviation and statistical tests for TimeAlign and second-best method (TVNet) on ETT, Weather, Electricity, Traffic and Solar datasets.

Local Align	Global Align		ETTm1		ETTm2		Weather		Electricity		Traffic	
w/	w/	Length	MSE	MAE	MSE	MAE	MSE	MAE	MSE	MAE	MSE	MAE
×	×	96	0.289	0.333	0.162	0.246	0.151	0.191	0.129	0.219	0.358	0.235
		192	0.328	0.358	0.221	0.287	0.193	0.231	0.146	0.235	0.377	0.245
		336	0.359	0.377	0.275	0.324	0.243	0.272	0.162	0.252	0.393	0.253
		720	0.420	0.412	0.349	0.375	0.314	0.323	0.200	0.284	0.431	0.273
		Avg.	0.349	0.370	0.252	0.308	0.225	0.254	0.159	0.248	0.390	0.249
✓	×	96	0.284	0.335	0.158	0.243	0.145	0.184	0.129	0.219	0.352	0.230
		192	0.324	0.359	0.212	0.282	0.188	0.226	0.145	0.235	0.372	0.239
		336	0.356	0.380	0.265	0.318	0.236	0.267	0.160	0.251	0.385	0.244
		720	0.414	0.415	0.345	0.375	0.310	0.319	0.196	0.282	0.425	0.265
		Avg.	0.344	0.372	0.245	0.305	0.220	0.249	0.157	0.247	0.383	0.244
×	✓	96	0.282	0.332	0.157	0.242	0.142	0.180	0.128	0.218	0.354	0.232
		192	0.325	0.358	0.211	0.281	0.184	0.223	0.146	0.234	0.369	0.236
		336	0.353	0.378	0.265	0.318	0.235	0.265	0.161	0.251	0.383	0.245
		720	0.409	0.410	0.343	0.371	0.311	0.320	0.193	0.280	0.424	0.265
		Avg.	0.342	0.369	0.244	0.303	0.218	0.247	0.157	0.246	0.383	0.245
✓	✓	96	0.279	0.330	0.155	0.241	0.140	0.179	0.126	0.216	0.349	0.225
		192	0.322	0.356	0.210	0.280	0.182	0.220	0.143	0.233	0.365	0.233
		336	0.350	0.375	0.263	0.315	0.232	0.262	0.158	0.249	0.377	0.240
		720	0.407	0.406	0.343	0.372	0.307	0.317	0.189	0.278	0.422	0.263
		Avg.	0.340	0.367	0.243	0.302	0.214	0.244	0.154	0.244	0.378	0.240

Table 8: Full results of ablation on the effect of removing alignment in local and global perspective. ✓ indicates the use of alignment, while × means alignment is retained.

Traffic datasets as in Fig. 8. The similarity maps of the ground truth and the reconstructed series are almost identical, with reconstruction errors approaching zero. This demonstrates that reconstruction effectively captures multi-frequency information, including both low-frequency periodic patterns and high-frequency variations, thereby assisting the forecaster in making more accurate predictions.

E.6 ROBUSTNESS ANALYSIS

For robustness against abrupt fluctuations, we also include experiments on high-volatility Stock Market data. It is well known that stock market data is extremely non-stationary, exhibiting evolving dynamics, abrupt regime changes, and distributional instability over time. To further evaluate robustness under distribution shifts, we conducted additional experiments on the two stock datasets (NASDAQ and NYSE) released by TFB (Qiu et al., 2024). As shown in Tab. 10, TimeAlign consistently achieves the best forecasting performance, outperforming all baselines across all prediction horizons. These findings further validate that our distilled “future prior” behaves reliably under distribution shifts, non-stationary temporal patterns, and evolving dynamics.

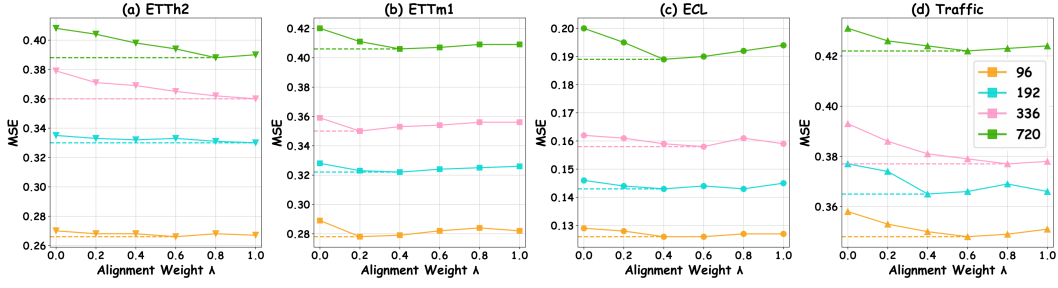


Figure 7: Effect of alignment loss weight across ETTh2, ETTm1, ECL and Traffic.

Models	iTransformer				+TimeAlign				DLLinear			+TimeAlign			
	Metric	MSE	MAE	SIM	MSE	MAE	SIM	ΔIMP	MSE	MAE	SIM	MSE	MAE	SIM	ΔIMP
ETTh1	96	0.300	0.353	0.880	0.302	0.352	0.883	-0.67%	0.300	0.345	0.887	0.300	0.342	0.888	+0.00%
	192	0.345	0.382	0.870	0.337	0.374	0.872	+2.32%	0.336	0.366	0.878	0.332	0.361	0.880	+1.19%
	336	0.374	0.398	0.859	0.364	0.389	0.863	+2.67%	0.367	0.386	0.863	0.362	0.380	0.867	+1.36%
	720	0.429	0.430	0.840	0.419	0.421	0.843	+2.33%	0.419	0.416	0.848	0.413	0.409	0.853	+1.43%
	Avg.	0.362	0.391	0.862	0.355	0.384	0.865	+1.80%	0.356	0.378	0.869	0.352	0.373	0.872	+1.05%
ETTh2	96	0.175	0.266	0.980	0.170	0.257	0.984	+2.86%	0.164	0.255	0.982	0.162	0.248	0.985	+1.22%
	192	0.242	0.312	0.974	0.234	0.298	0.979	+3.31%	0.224	0.304	0.977	0.218	0.287	0.979	+2.68%
	336	0.282	0.340	0.969	0.278	0.332	0.972	+1.42%	0.277	0.337	0.971	0.270	0.325	0.975	+2.53%
	720	0.378	0.398	0.956	0.358	0.381	0.961	+5.29%	0.371	0.401	0.960	0.359	0.385	0.963	+3.23%
	Avg.	0.269	0.329	0.970	0.260	0.317	0.974	+3.44%	0.259	0.324	0.973	0.252	0.311	0.976	+2.61%
ETTh3	96	0.386	0.405	0.849	0.382	0.412	0.853	+1.04%	0.379	0.403	0.862	0.367	0.394	0.861	+3.17%
	192	0.424	0.440	0.833	0.420	0.439	0.836	+0.94%	0.408	0.419	0.848	0.406	0.416	0.846	+0.49%
	336	0.449	0.460	0.823	0.447	0.458	0.825	+0.45%	0.440	0.440	0.838	0.432	0.440	0.835	+1.82%
	720	0.495	0.487	0.795	0.462	0.482	0.799	+6.67%	0.471	0.493	0.816	0.452	0.480	0.819	+4.03%
	Avg.	0.439	0.448	0.825	0.428	0.448	0.828	+2.45%	0.424	0.439	0.841	0.414	0.433	0.840	+2.41%
ETTh2	96	0.297	0.348	0.967	0.288	0.349	0.971	+3.03%	0.289	0.353	0.970	0.283	0.344	0.970	+2.08%
	192	0.371	0.403	0.959	0.361	0.395	0.963	+2.70%	0.383	0.418	0.962	0.362	0.396	0.962	+5.48%
	336	0.404	0.428	0.954	0.394	0.421	0.959	+2.48%	0.448	0.465	0.956	0.420	0.439	0.957	+5.36%
	720	0.424	0.444	0.950	0.410	0.442	0.953	+3.30%	0.605	0.551	0.950	0.607	0.545	0.951	-0.33%
	Avg.	0.374	0.406	0.958	0.363	0.402	0.962	+2.87%	0.431	0.447	0.960	0.418	0.431	0.960	+3.07%
Weather	96	0.159	0.208	0.852	0.160	0.203	0.858	-0.63%	0.170	0.230	0.848	0.169	0.223	0.845	+0.59%
	192	0.200	0.248	0.798	0.209	0.248	0.809	-4.50%	0.216	0.273	0.805	0.210	0.256	0.805	+2.78%
	336	0.253	0.289	0.751	0.258	0.294	0.758	-1.98%	0.258	0.307	0.760	0.255	0.294	0.758	+1.16%
	720	0.321	0.338	0.706	0.334	0.350	0.682	-4.05%	0.323	0.362	0.698	0.318	0.346	0.692	+1.55%
	Avg.	0.233	0.271	0.777	0.240	0.274	0.777	-3.00%	0.242	0.293	0.778	0.238	0.280	0.775	+1.55%
Electricity	96	0.138	0.237	0.932	0.132	0.225	0.936	+4.35%	0.140	0.237	0.927	0.137	0.234	0.932	+2.14%
	192	0.157	0.256	0.920	0.154	0.247	0.923	+1.91%	0.152	0.249	0.919	0.151	0.247	0.923	+0.66%
	336	0.167	0.264	0.908	0.169	0.262	0.910	-1.20%	0.169	0.267	0.911	0.167	0.263	0.914	+1.18%
	720	0.194	0.286	0.895	0.196	0.284	0.893	-1.03%	0.203	0.301	0.891	0.201	0.295	0.893	+0.99%
	Avg.	0.164	0.261	0.914	0.163	0.255	0.916	+0.76%	0.166	0.264	0.912	0.164	0.260	0.916	+1.20%
Traffic	96	0.363	0.265	0.854	0.354	0.242	0.857	+2.48%	0.395	0.275	0.838	0.397	0.275	0.837	-0.51%
	192	0.385	0.273	0.848	0.377	0.255	0.852	+2.08%	0.407	0.280	0.836	0.406	0.278	0.835	+0.25%
	336	0.396	0.277	0.845	0.399	0.264	0.846	-0.76%	0.417	0.286	0.834	0.416	0.283	0.836	+0.24%
	720	0.445	0.308	0.831	0.428	0.279	0.837	+3.82%	0.454	0.308	0.821	0.452	0.302	0.822	+0.44%
	Avg.	0.397	0.282	0.845	0.390	0.260	0.848	+1.95%	0.418	0.287	0.832	0.418	0.285	0.833	+0.12%
Solar	96	0.188	0.232	0.860	0.181	0.230	0.866	+3.72%	0.197	0.210	0.854	0.190	0.203	0.858	+3.55%
	192	0.193	0.248	0.852	0.205	0.249	0.851	-6.22%	0.218	0.222	0.849	0.212	0.217	0.854	+2.75%
	336	0.203	0.249	0.850	0.218	0.250	0.848	-7.39%	0.234	0.231	0.846	0.224	0.223	0.851	+4.27%
	720	0.223	0.261	0.845	0.210	0.244	0.847	+5.83%	0.243	0.241	0.844	0.229	0.233	0.846	+5.76%
	Avg.	0.202	0.248	0.852	0.204	0.243	0.853	-0.87%	0.224	0.226	0.848	0.214	0.219	0.852	+4.15%

Table 9: Full results of long-term forecasting with TimeAlign as a plugin. All results are averaged across four different prediction lengths: $O \in \{96, 192, 336, 720\}$. ΔIMP denotes TimeAlign’s performance gain, either *positive* or *negative*.

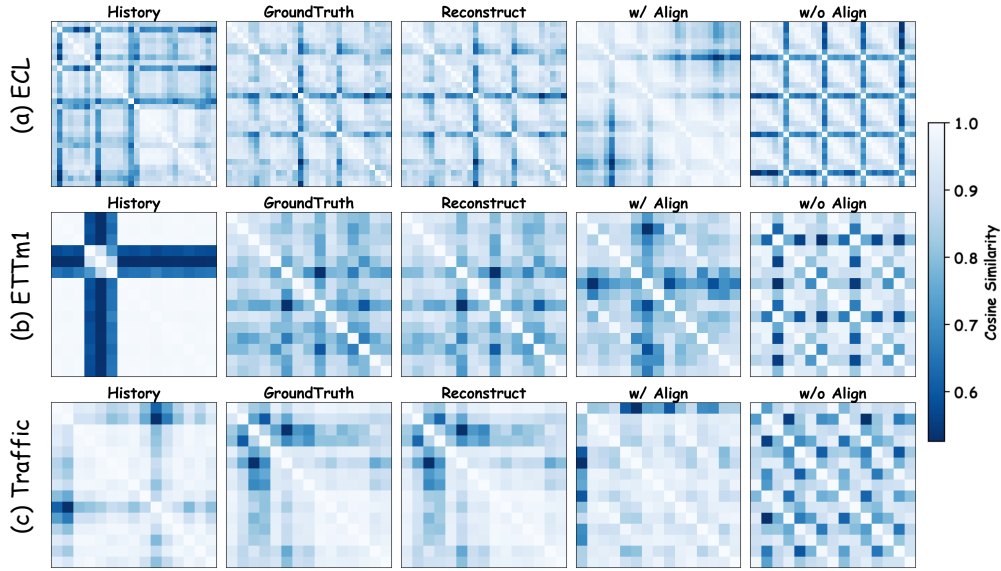


Figure 8: Visualization of patch-wise similarity of history, ground truth, reconstructed series, forecast with and without alignment from ETTm1, ECL and Traffic. The similarity maps of the ground truth and the reconstructed series are almost identical, with reconstruction errors approaching zero.

Models	TimeAlign (Ours)		PatchTST (2023)		Crossformer (2023)		DLinear (2023)		NLinear (2023)		MICN (2022)		TimesNet (2023)		FEDformer (2022)	
	MSE	MAE	MSE	MAE	MSE	MAE	MSE	MAE	MSE	MAE	MSE	MAE	MSE	MAE	MSE	MAE
NASDAQ	0.649	0.879	0.717	0.977	0.999	1.752	0.889	1.503	<u>0.682</u>	0.926	0.884	1.530	0.697	0.996	0.694	<u>0.900</u>
NYSE	0.385	0.388	0.427	0.471	0.913	0.988	0.526	0.582	<u>0.401</u>	<u>0.402</u>	0.639	0.737	0.475	0.509	0.422	0.407

Table 10: Long-term forecasting results on stock market data.

E.7 HIGH FREQUENCY ANALYSIS

To directly validate TimeAlign’s capability to capture rapid temporal dynamics, we introduce the High-Frequency Mean Squared Error ($\mathcal{L}_{\text{HF-MSE}}$). This metric quantifies the error between the predicted (\hat{Y}) and true (Y) series in the frequency domain, focusing only on the high-frequency band ($\mathcal{S}_{\text{high}}$) identified via knee-point detection. Calculation of HF-MSE: The metric is computed by performing the Discrete Fourier Transform (DFT) on Y and \hat{Y} and calculating the mean squared magnitude difference on the isolated high-frequency components:

$$\mathcal{L}_{\text{HF-MSE}} = \frac{1}{T_{\text{high}}} \sum_{k \in \mathcal{S}_{\text{high}}} \left| (Y_{\text{freq}})_k - (\hat{Y}_{\text{freq}})_k \right|^2$$

where T_{high} is the count of components in $\mathcal{S}_{\text{high}}$. Tab. 11 summarizes the improvement in HF-MSE across datasets and presents results on various datasets, demonstrating the superior robustness of TimeAlign on abrupt, fine-grained temporal dynamics.

E.8 EXTRA ANALYSIS OF DISTRIBUTION-AWARE ALIGNMENT

Influence of Alignment Loss Weight. We further investigate the influence of the key hyperparameter, the weight of alignment loss λ , sweeping $\lambda \in \{0.0, 0.2, 0.4, 0.6, 0.8, 1.0\}$ across four datasets. Fig. 7 shows that ETTh2 and ETTm1 are highly sensitive to λ , whereas ECL and Traffic remain relatively stable. In essence, λ controls the trade-off between distribution matching and point-wise error minimization. As λ increases, the model increasingly emphasizes aligning the predictive and target distributions, a strategy that generally reduces error, since better distribution overlap typically

Models	ETTh1		ETTm1		Weather		ECL		Traffic	
	HF-MSE	HF-MAE	HF-MSE	HF-MAE	HF-MSE	HF-MAE	HF-MSE	HF-MAE	HF-MSE	HF-MAE
TimeAlign	2.86	1.27	2.54	1.19	3.51	1.35	40.60	5.09	253.71	10.64
w/o Align	2.97	1.36	2.73	1.35	3.66	1.50	42.75	5.44	261.43	11.56

Table 11: Long-term forecasting results with HF-MSE/HF-MAE metrics.

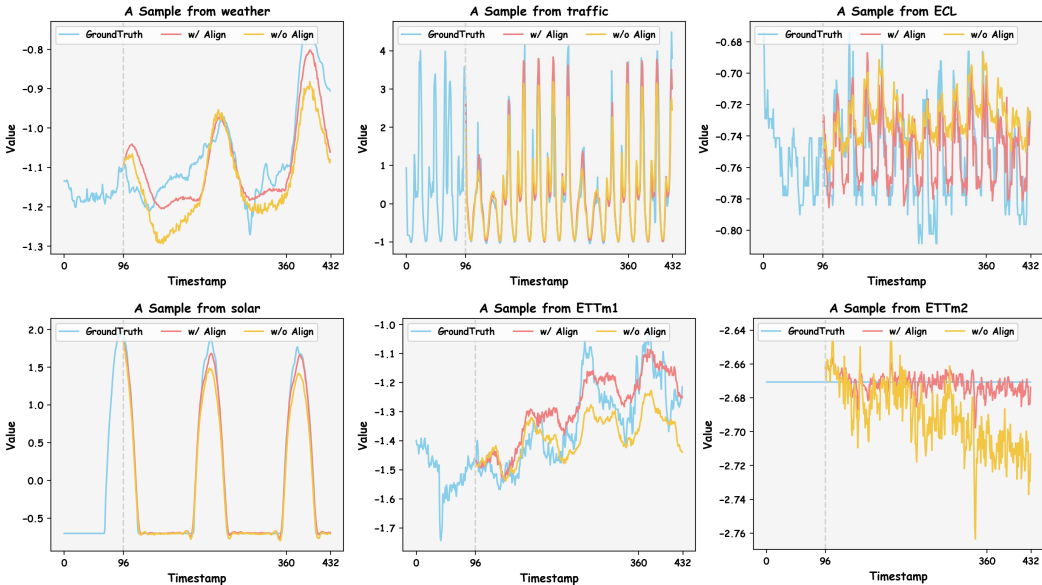


Figure 9: Visualization of predictions from ETTm1, ETTm2, ECL, Solar and Traffic.

implies lower error. However, an excessively high λ may cause the model to highlight minority modes, particularly outliers, thereby degrading performance. Therefore, selecting an appropriate λ for each dataset amounts to carefully balancing these two optimization objectives to maximize the overall predictive capability.

F VISUALIZATION

In order to facilitate a clear comparison between with and without alignment, we present supplementary prediction examples for four datasets, as ETTm1, ETTm2, Weather, ECL, Solar, and Traffic in Fig. 9, respectively. The look-back horizon L and the forecasting horizon T are both 720 for all four datasets.